

# Forward modeling and retrieval of water vapor from the Global Ozone Monitoring Experiment: Treatment of narrowband absorption spectra

Rüdiger Lang,<sup>1,2</sup> Ahilleas N. Maurellis,<sup>3</sup> and Wim J. van der Zande  
FOM Institute for Atomic and Molecular Physics, Amsterdam, Netherlands

Ilse Aben and Jochen Landgraf  
SRON National Institute for Space Research, Utrecht, Netherlands

Wim Ubachs  
Department of Physics and Astronomy, Vrije Universiteit, Amsterdam, Netherlands

Received 1 November 2001; revised 10 December 2001; accepted 10 December 2001; published 27 August 2002.

[1] We present the algorithm and results for a new fast forward modeling technique applied to the retrieval of atmospheric water vapor from satellite measurements using a weak ro-vibrational overtone band in the visible. The algorithm uses an Optical Absorption Coefficient Spectroscopy (OACS) method which is well suited to situations where line widths in the absorption spectrum are much narrower than the instrumental resolution and where efficient numerical solutions of the equation of radiative transfer are needed. We present examples of OACS forward modeled reflectivity which include the differential contribution of singly scattered photons and compare them with spectral measurements of the Global Ozone Monitoring Experiment (GOME). In particular, we apply OACS to the retrieval of water vapor column (WVC) densities from GOME spectral data between 585 and 600 nm. Method precisions are better than 0.7% for high and better than 3.4% for low WVC. The total accuracy of the retrieval method appears to be better than 0.8 and 4% for high and low WVC, respectively. The retrieval results are compared to WVC values given by European Centre for Medium-Range Weather Forecasts and Special Sensor Microwave Imager and allow us to conclude that the OACS retrieval method is reliable except in cloud-rich situations. In cloud-free cases, an upper limit of 18% error on the retrieved WVC due to the impact of multiple and aerosol scattering as well as aerosol extinction is estimated. In addition, the accuracy of the retrieval is sufficient to permit the detection of systematic differential fit mismatches between modeled and real GOME spectra. The magnitude of such mismatches places an upper limit on the accuracy of HITRAN'96 water vapor line strength values of about 10–20%. *INDEX TERMS:* 0933

Exploration Geophysics: Remote sensing; 0360 Atmospheric Composition and Structure: Transmission and scattering of radiation; 0365 Atmospheric Composition and Structure: Troposphere—composition and chemistry; 3210 Mathematical Geophysics: Modeling; 3260 Mathematical Geophysics: Inverse theory; *KEYWORDS:* water vapor, retrieval, GOME, sampling technique, spectroscopy

## 1. Introduction

[2] Spectroscopic measurements from satellite-based instruments covering relatively broad wavelength regions may be used to affect column and vertical profile retrieval

for many different atmospheric constituents. The Global Ozone Monitoring Experiment (GOME) spectrometer on the European Space Agency's ERS-2 satellite [*European Space Agency (ESA)*, 1995; *Burrows et al.*, 1999] covers a wavelength region between 240 and 790 nm. In this wavelength region absorption bands of many constituents such as, for example, O<sub>2</sub>, NO<sub>2</sub>, H<sub>2</sub>O, O<sub>3</sub>, (O<sub>2</sub>)<sub>2</sub>, and OCIO are measurable. Column concentration retrieval is routinely carried out for O<sub>3</sub> and NO<sub>2</sub> (level 2 products). Important information about OCIO, volcanic SO<sub>2</sub>, H<sub>2</sub>CO from biomass burning and tropospheric BrO, has also been delivered [*Thomas et al.*, 1998].

[3] The Scanning Imaging Absorption Spectrometer for Atmospheric Cartography (SCIAMACHY) [*Bovensmann*

<sup>1</sup>Also at Space Research Organization Netherland, Utrecht, Netherlands.

<sup>2</sup>Also at Department of Physics and Astronomy, Vrije Universiteit, Amsterdam, Netherlands.

<sup>3</sup>Now at SRON National Institute for Space Research, Utrecht, Netherlands.

*et al.*, 1999] will be launched on ENVISAT in 2001 and will extend wavelength coverage into the near infrared up to 1750 nm while adding two additional channels in regions between 1.9 and 2.4 microns. Thus GOME's list of targeted species will be extended to include CO, CO<sub>2</sub>, N<sub>2</sub>O and CH<sub>4</sub>. The absorption features of some of these gases are often contaminated by strong water vapor absorption bands [Schrijver, 1999; Buchwitz *et al.*, 2000]. Retrieval of such species would thus require fast forward modeling of the water vapor using the results of a sensitive retrieval method retrieving water vapor column (WVC) concentrations, for example in the visible region of the instrument.

[4] This paper focuses on the retrieval of WVC from GOME measurements in the visible between 585 and 600 nm. This relatively weak absorption window was first described by *Maurellis et al.* [2000a]. It contains additional absorption features due to sodium, the ozone Chappuis band, the (O<sub>2</sub>)<sub>2</sub> collision complex, which we account for in this work as well as a weak contribution of NO<sub>2</sub>. In contrast, the most prominent water vapor absorption band covered by the GOME detectors is at 720 nm. This band contains, on average, features which are up to an order of magnitude more optically dense than the strongest features in the weak 590 nm band. Nevertheless, we expect that the reflectivity measured in the 720 nm region is less sensitive to changes in pressure and temperature over altitude. Due to the strong absorption in the line center and the strong overlap of the line wings in the lower troposphere, at high pressures and high water vapor content, the 720 nm region is less sensitive to changes in WVC. In this paper we present a new method called Optical Absorption Coefficient Spectroscopy (OACS) which allows both for fast and accurate forward modeling of GOME reflectivity measurements affected by water vapor absorption as well as relatively fast retrievals of WVC.

[5] Until recently the retrieval of WVC from GOME measurements was not successful without the introduction of substantial modification [Noël *et al.*, 1999; Casadio *et al.*, 2000] to differential methods such as the Differential Optical Absorption Spectroscopy method (DOAS) [Platt, 1994, 1999] used for the retrieval of GOME level 2 products [Burrows *et al.*, 1999]. In principle DOAS operates by separating out the broadband absorption structure due to elastic scattering or broadband absorption from the differential structure of the trace gas under study in order to fit Beer's Law to a measured reflectivity spectrum. DOAS offers a good compromise between speed, numerical accuracy and instrument performance and has repeatedly proven its usefulness for many molecular species. However it is frequently combined with a simple arithmetic wavelength-averaging of optical densities for broadband absorbers in order to establish a linear dependence between the logarithm of the measured reflectivity and the fit parameters [Marquard *et al.*, 2000; Burrows *et al.*, 1999]. In this case, the retrieval of the atmospheric water vapor concentrations would result in a systematic underestimation of the expected WVC due to an inadequate sampling of highly varying optical densities by a single detector pixel [Maurellis *et al.*, 2000a, 2000b]. In addition, discrepancies may also arise out of inadequate treatment of air mass factors used to account for the contribution of atmospheric scattering [Noël *et al.*, 1999; Casadio *et al.*, 2000].

[6] It is important to make the distinction between narrow-band and broadband absorbers in the context of a spectral fitting window in order to separate the reflectivity contribution of absorbers with strong differential structure from the relatively smooth background. In addition to coping with intrinsic spectral complexity the retrieval of atmospheric trace gas columns also requires accurate spectral information as well as spectrometers which operate at sufficient spectral resolution. However, spectral coverage (i.e., the potential to retrieve a wide variety of atmospheric constituents using a single instrument) usually has to be compromised by a reduction in spectral resolution. For example, two linear array detectors with 1024 detector pixels each are needed in order to cover the wavelength range of the Ozone Chappuis band between 400 and 800 nm using the GOME instrument (channel three and four), where each detector pixel covers a wavelength range of about 0.2 nm. The spectral sampling is sufficient to resolve spectral absorption features of many species especially in the near ultraviolet where line-broadening by predissociation of excited molecular states causes the optical density to vary little within the span of a single detector pixel (for example in the case of ozone). In contrast, many species with absorption bands in the visible and near-infrared (for example, water vapor, NO<sub>2</sub>, methane, or atomic species like sodium) lack smoothing from line-broadening and may contain a number of distinct absorption lines within the wavelength region covered by one detector pixel. This also holds for wide parts of the solar irradiance spectrum over the entire ultraviolet and visible regions which contains narrowband Fraunhofer absorption lines.

[7] The fast forward modeling and retrieval method presented here focuses on the problem of spectral sampling in cases of such narrowband absorption spectra. This means that the spectral width of the instrumental function and the sampling width of the detector is much broader than the width of a single absorption line. In such cases a convolution and sampling integral over the modeled highly structured reflectivity spectra has to be introduced when modeling the spectra measured by an instrument with insufficient sampling capacity. The proposed Optical Absorption Coefficient Method (OACS) shows that this problem can be solved accurately and with sufficient efficiency that, using operational data from GOME in the visible, the water vapor column (WVC) retrieved is comparable to other fundamental different satellite measurement techniques and data assimilation models [Vesperini, 1998; Chaboureau *et al.*, 1998].

[8] The problem of the treatment has also been dealt with by a new Spectral Structure Parameterization (SSP) method [Maurellis *et al.*, 2000b]. In the latter work it was shown that the complexity of spectra ranging from single line absorption to broadband absorption may be characterized, to second order in accuracy, by a simple parameterization scheme. In what follows we show that the OACS retrieval method permits both fast and accurate forward modeling of reflectivities as well as relatively fast retrievals of trace gas concentrations.

[9] In principle, an OACS retrieval method could take advantage of the DOAS method in the sense that it could utilize a first-order polynomial in order to account for the unknown surface albedo as well as the non-structured background contribution of atmospheric scattering. However, in order to account for the contribution of single-

scattered photons, we show that a more accurate representation can be obtained in the form of an additional OACS term derived from the solution of the equation of radiative transfer. However, the contribution of multiple scattering can be significant in the visible region covered by this instrument. Therefore a polynomial similar to the one used in standard DOAS methods is introduced to account for the broadband contribution of multiple-scattered photons. The influence of the neglected differential contribution of the latter on the modeled reflectivities as well as fit residuals and retrieved WVCs has to be estimated and discussed in some detail. However, apart from these assumptions, OACS already displays the ability to retrieve WVCs for low cloud cover situations with an accuracy of state-of-the-art products like the ones from the European Center of Medium Range Weather Forecast (ECMWF) and the Special Sounder Microwave Imager (SSM/I). In addition, this first extensive study retrieving water vapor from GOME operational data in the visible shows the potential of OACS to be applied to WVC retrieval from the forthcoming SCIAMACHY instrument especially in the infrared.

[10] In section 2 we introduce the radiation transport scheme on which OACS is based together with the mathematical formulation of the method. Section 4 Measurements briefly describes the GOME instrument performance and how GOME-measured earth radiances and solar irradiances are handled for the purposes of WVC retrieval. The issue of undersampling and the specific definition of reflectivity used for retrievals from GOME data are also presented. In section 5 the HITRAN'96 water vapor line-strength values used in the OACS method are described in some detail since the method's sensitivity to changes in the reflectivity with respect to the cross-section of the trace gas under study requires an accurate knowledge of the line parameters and their dependence on the pressure and temperature for a specific geolocation. A retrieval of WVCs from an entire water vapor absorption band requires accurate modeling of all additional absorbers within this band in order to prevent the fit from confusing part of the instrumentally smoothed water vapor absorption spectrum with the background. An introduction in the modeling of this background together with a description of the required input data is also given in section 5. Section 6 estimates the intrinsic OACS method-related error due to the specific sampling of the intensities. Section 7 describes the forward modeling of GOME spectral measurements using the OACS method. The results are compared to an independent solution of the equation of radiative transfer using a doubling-adding model (DAM) [de Haan *et al.*, 1987]. In section 8 the effect on the retrieved WVC due to the differential contribution of photons scattered more than once in the atmosphere (multiple scattering) as well as aerosol scattering and absorption are discussed and quantified using results of the DAM model. In section 9 we estimate the precision and the accuracy of the method by retrieving WVCs from artificial absorption spectra which are forward modeled using a 1b1 calculation. Here we also present a study of the influence of multiple scattering and aerosol loading on the retrieved WVC. The results of WVC-retrieval from three different GOME tracks are presented in section 10. In this section we also discuss the impact of differential fit mismatches on the residuals and the retrieved WVCs which we relate predominantly to instrumental errors

**Table 1.** Summary of Some of the Most Important Notations Used in This Paper

Sign	Description
k	A. c. <sup>a</sup> with broadband X-s. <sup>b</sup>
f	A. c. with narrowband X-s.
$\ell$	Atmospheric layer
$\mu_o, \mu$	Incoming and outgoing angle cosine
j	Detector pixel number
i	Cross-section bin
$\bar{\alpha}_{ij}^{(\ell)}$	Alpha value interpolated in $p, T$
$\xi_i$	X-s. bin center value
$\Sigma$	Instrument slit-width
$\Delta\lambda$	Detector pixel width
$\gamma$	WV-line HWHM
$\delta\lambda$	Grid size reference spectra
$I, I_0$	Specific intensities
R	Reflectivity ( $=\pi(\mu_o)/I_0$ )
$\Lambda$	Surface albedo
$S_{\bar{v}}$	Line-strength
$\Delta\phi$	Differential fit mismatch correction

<sup>a</sup> Atmospheric constituent.

<sup>b</sup> Cross-section.

and to errors in the water vapor line-strength values taken from the HITRAN'96 database. A preliminary validation of the OACS retrieval results using ECMWF and SSM/I data is set out in section 11. The latter is discussed in conjunction with the effect of clouds. Finally, in section 12, we focus on potential implementation of the OACS method in routine retrieval and its use for forward modeling of water vapor absorption bands in spectral regions containing narrowband absorption features other than water vapor.

## 2. Radiative Transfer

[11] The transport equation of scalar radiative transfer in its plane parallel approximation is given by

$$\mu \frac{dI_{\lambda}}{dz}(z, \Omega) = -\beta_{\text{ext}}(z) \{I_{\lambda}(z, \Omega) - J_{\lambda}(z, \Omega)\} \quad (1)$$

where  $I_{\lambda}$  is the specific intensity field for a given wavelength  $\lambda$ ,  $J_{\lambda}$  is the corresponding source function and  $\beta_{\text{ext}}$  is the extinction coefficient (see Table 1). Further,  $z$  represents the altitude and  $\Omega$  is the direction of the intensity field with  $\Omega = (u, \varphi)$ , where  $\mu = |u|$  is the cosine of the zenith angle.  $I_{\lambda}$  is subject to boundary conditions at the top and bottom of the atmosphere ( $z = 0$  and  $z_{\text{top}}$ ), respectively, of the form

$$I_{\lambda}(z_{\text{top}}, \Omega_{-}) = 0 \quad (2)$$

$$I_{\lambda}(0, \Omega_{+}) = \frac{\lambda}{\pi} F^{\downarrow} \quad (3)$$

for which we have assumed isotropic ground reflection by a Lambertian surface with an albedo  $\Lambda$ . Here,  $\Omega_{+}$  and  $\Omega_{-}$  indicate upward and downward directions, respectively, and  $F^{\downarrow}$  is the downward flux at the lower boundary of the atmosphere,

$$F^{\downarrow} = \int_{\Omega_{-}} I(0, \Omega) \mu \, d\Omega. \quad (4)$$

Neglecting multiple scattering in the visible part of the solar spectrum, the source function is given by

$$J_{\lambda(z,\Omega)} = F_o \frac{\beta_{\text{sca}}(z)}{\beta_{\text{ext}}(z)} P(z, \Omega_o, \Omega) e^{-\tau(z)/\mu_o} \quad (5)$$

where  $\beta_{\text{sca}}$  is the scattering coefficient,  $F_o$  is the incoming solar flux,  $P$  is the scattering phase function and  $\Omega_o, \mu_o$  describes the solar geometry. The optical depth  $\tau$  is defined by

$$\tau(z) = \int_0^z \beta_{\text{ext}}(z') dz'. \quad (6)$$

[12] Thus, in the single scattering approximation, the radiative transfer equation (1) can be integrated easily, which provides the reflected intensity field at the top of the atmosphere as a function of the boundary condition (3),

$$I_{\lambda}(z_{\text{top}}, \Omega) = I_{\lambda}(0, \Omega) e^{-\tau(0)/\mu} + \frac{F_o}{\mu} \int_0^{z_{\text{top}}} \beta_{\text{sca}}(z) e^{-\tau(z)\frac{\mu_o+\mu}{\mu_o\mu}} P(z, \Omega, \Omega_o) dz \quad (7)$$

If we further assume that the downward flux  $F_{\leftrightarrow}$  in (3) is dominated by its direct beam contribution

$$F^{\downarrow} \approx \mu_o F_o e^{-\tau(0)/\mu_o}, \quad (8)$$

we can approximate the specific intensity in the viewing direction of the satellite with

$$I_{\lambda}(z_{\text{top}}, \Omega) = \frac{\lambda}{\pi} \mu_o F_o e^{-\tau(0)\frac{\mu_o+\mu}{\mu_o\mu}} + \frac{F_o}{\mu} \int_0^{z_{\text{top}}} \beta_{\text{sca}}(z) e^{-\tau(z)\frac{\mu_o+\mu}{\mu_o\mu}} P(z, \Omega, \Omega_o) dz \quad (9)$$

[13] Let us now assume that Rayleigh scattering is the dominant form of single-scattering. In this case we may write the scattering coefficient  $\beta_{\text{sca}}(z, \lambda)$  as,

$$\beta_{\text{sca}}(z, \lambda) = \sigma_R(\lambda) \sum_{k=1}^K n_k(z). \quad (10)$$

[14] Here  $n_k$  denotes the density of the  $k$ th species and  $\sigma_R(\lambda)$  is the Rayleigh scattering cross-section with a corresponding phase function of

$$P(\Omega_o \rightarrow \Omega) = p(\theta) = \frac{3}{4}(1 + \cos^2 \theta), \quad (11)$$

satisfying

$$\frac{1}{4\pi} \int p'(\Omega \rightarrow \Omega') d\Omega = 1. \quad (12)$$

[15] We now consider a satellite instrument which spectrally redistributes incoming intensities because of the slit in the path of the optics. The result is, that the detectors sample

a smoothed intensity. We assume that this may be accounted for by convolving the measured intensity using an instrumental response function  $\mathcal{H}(\lambda, \lambda'; \Sigma)$  with a spectral  $\sigma$ -width  $\Sigma$ . After the convolution is performed the intensity is sampled by simply averaging over the wavelength region  $\Delta\lambda$  covered by one detector pixel. In addition we assume that the differential contribution of Fraunhofer line absorption in the measured solar irradiance is negligible. By dividing  $I \equiv I_{\lambda}(z_{\text{top}}, \Omega)$  from equation (9) with  $\mu_o F_o$  we write the unitless normalized reflectivity  $R$  measured by a single detector pixel  $j$  as

$$R_j = \int_{\Delta\lambda_j} \int_{-\infty}^{+\infty} \frac{\pi I}{\mu_o F_o} \mathcal{H}(\lambda, \lambda'; \Sigma) d\lambda' \frac{d\lambda}{\Delta\lambda_j}. \quad (13)$$

[16] Here, the outermost wavelength integral takes place over detector pixel wavelength range  $\Delta\lambda_j$ . For convenience it is possible to separate equation (13) into a pure surface reflectance and an atmospheric single-scattering part,  $R_j = R_{\text{surf},j} + R_{\text{ss},j}$ , using equation (9) with  $\tilde{\mu} \equiv (\frac{1}{\mu_o} + 1)$  in the case of a nadir viewing instrument ( $\mu = 1$ ), such that

$$R_{\text{surf},j} = \Lambda \int_{\Delta\lambda_j} \int_{-\infty}^{+\infty} e^{-\tau(z_o, \lambda')\tilde{\mu}} \mathcal{H}(\lambda, \lambda'; \Sigma) d\lambda' \frac{d\lambda}{\Delta\lambda_j} \quad (14)$$

accounts for the reduced intensity of the measured light reflected at the ground level by absorption and scattering out of the light path and

$$R_{\text{ss},j} = \frac{p(\theta)}{4\mu_o} \int_{\Delta\lambda_j} \int_{-\infty}^{+\infty} \left[ \int_0^{\infty} \beta_{\text{sca}}(z, \lambda') e^{-\tau(z, \lambda')\tilde{\mu}} dz \right] \times \mathcal{H}(\lambda, \lambda'; \Sigma) d\lambda' \frac{d\lambda}{\Delta\lambda_j} \quad (15)$$

accounts for light undergoing single-scattering at each altitude  $z$ . We now separate the various absorbers into constituents  $k$ , for which the change in cross-section within the wavelength region  $\Delta\lambda$  is very small (for example the Rayleigh scattering cross section  $\sigma_R$ ) and constituents  $f$  with narrowband cross-sections within  $\Delta\lambda$ . In the case of  $\Delta\lambda \ll \Sigma$  we may exchange the position of the sampling and the convolution integral and write equations (14) and (15) as

$$R_{\text{surf},j} = \Lambda \int_{-\infty}^{+\infty} \left\{ e^{-\sum_{k=1}^K \int_{z_0}^{\infty} \bar{\sigma}_k(z') n_k(z') \tilde{\mu} dz'} \times \int_{\Delta\lambda_j} e^{-\sum_{f=1}^F \int_{z_0}^{\infty} \sigma_f(z', \lambda) n_f(z') \tilde{\mu} dz'} \frac{d\lambda}{\Delta\lambda_j} \right\} \times \mathcal{H}(\lambda, \lambda'; \Sigma) d\lambda', \quad (16)$$

and

$$R_{\text{ss},j} = \frac{p(\theta)}{4\mu_o} \int_{-\infty}^{+\infty} \left\{ \int_0^{\infty} [\beta_{\text{sca}}(z, \lambda')] \times e^{-\sum_{k=1}^K \int_z^{\infty} \bar{\sigma}_k(z') n_k(z') \tilde{\mu} dz'} \times \int_{\Delta\lambda_j} e^{-\sum_{f=1}^F \int_z^{\infty} \sigma_f(z', \lambda) n_f(z') \tilde{\mu} dz'} \frac{d\lambda}{\Delta\lambda_j} \right\} dz \times \mathcal{H}(\lambda, \lambda'; \Sigma) d\lambda'. \quad (17)$$

Here  $\bar{\sigma}_k$  is the arithmetic mean cross-section of the  $k$ th absorber with a low-frequency spectral-structure within  $\Delta\lambda$ . The problem remains to formulate the innermost integral, i.e. the sampling term over the high frequency components, in a way that is still suitable for a relatively fast forward modeling and fitting.

### 3. Optical Absorption Coefficient Spectroscopy

[17] Recently a new opacity-sampling technique was proposed [Maurellis, 1998] which rapidly evaluates the wavelength-averaged Lambert-Beer's Law transmittance due to any general line or continuum absorption spectrum in a non-grey atmosphere. It utilizes numerical realizations of pressure- and temperature-dependent absorption cross sections in order to compute the non-normalized discretized probability density function (pdf), denoted  $\alpha_{ij}$ , of the cross-section at a value of  $\xi_i$ , over a wavelength range  $\Delta\lambda$ . The pdf thus carries the information of the detailed spectral structure as a function of absorption cross-section  $\xi_i$  within the wavelength range of a detector pixel  $j$  and satisfies

$$\int_{\Delta\lambda_j} \sigma(\lambda) d\lambda \approx \sum_{i \in \mathcal{R}} \alpha_{ij} \xi_i \delta\lambda.$$

$\mathcal{R}$  denotes an ordered, non-overlapping set of bin indices covering the full range of possible values of the absorption cross-section and with bin centers given by the values of  $\xi_i$ .

[18] It has been shown [Maurellis, 1998] that the Beer's law component of a one-species form of equation (14) may be expressed without the convolution in the integral as

$$\int_{\Delta\lambda_j} \exp\left(-\int_{\infty}^z \sigma(\lambda, z') n(z') dz'\right) \frac{d\lambda}{\Delta\lambda_j} \approx \sum_{i \in \mathcal{R}} \eta_{ij} \exp\left[-\xi_i \int_{\infty}^z n(z') dz'\right] \frac{\delta\lambda}{\Delta\lambda_j}, \quad (18)$$

where

$$\eta_{ij} = \frac{\int_{\infty}^z \alpha_{ij}(z') n(z') dz'}{\int_{\infty}^z n(z') dz'}$$

The wavelength grid size,  $\delta\lambda$ , is the crucial parameter in the trade-off between computational speed and the accuracy of the representation in equation (18). We choose  $\delta\lambda = 2 \times 10^{-3} \Delta\lambda$  in this work. Next, the integral over path  $S$  may be altitude-discretized by writing it as a summation over a series of atmospheric layers  $\ell$  with column densities  $N_\ell$  (see Figure 1), viz.

$$\int_{\Delta\lambda_j} \exp\left(-\int_{\infty}^z \sigma(\lambda, z') n(z') dz'\right) \frac{d\lambda}{\Delta\lambda_j} \approx \sum_i \bar{\eta}_{ij}^\ell \exp\left(-\xi_i \sum_{\ell=1}^L N_\ell\right) \frac{\delta\lambda}{\Delta\lambda_j}, \quad (19)$$

where

$$\bar{\eta}_{ij}^\ell = \frac{\sum_{\ell=1}^L \bar{\alpha}_{ij}^{(\ell)} N_\ell}{\sum_{\ell=1}^L N_\ell},$$

and  $\bar{\alpha}_{ij}^{(\ell)} = \alpha_{ij}(T_\ell(z_\ell), p_\ell(z_\ell))$ . In this formulation  $N_\ell$  contains an implicit multiplicative factor which accounts for the greater

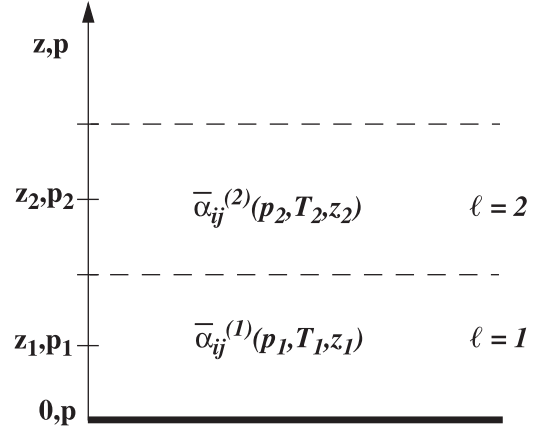


**Figure 1.** Each atmospheric layer  $\ell$  is defined such that the values for pressure  $p_\ell$  and temperature  $T_\ell$  at altitude  $z_\ell$  of a given profile are the mean values of each layer  $\ell$ . In this way  $\bar{\alpha}_{ij}^{(\ell)}(p_\ell, T_\ell)$  represents the mean coefficient values for each layer  $\ell$  interpolated in pressure and temperature from the  $\alpha_{ij}(p, T)$ -table, where  $p$  and  $T$  are taken from a fixed grid of pressures and temperatures used for the construction of the table.

air mass traversed by non-zero solar zenith angle photons. In all calculations we assume that this air mass correction factor is determined simply by spherical geometry.

[19] The use of equation (19) to replace the spectral sampling integral we call an Opacity Coefficient Method (OCM). The coefficients  $\bar{\alpha}_{ij}^{(\ell)}$  represent the probability density function for cross-section averaged out over each atmospheric level  $\ell$ . In practice they are determined from spectral realizations (see section 5) for each detector pixel  $j$  which have been pre-calculated for a range of temperatures and pressures. These pre-calculations are used to compile an  $\alpha_{ij}(p, T)$  table for every combination of  $i$  and  $j$ . Independently acquired temperature and pressure profiles (in terms of an altitude grid  $\{z_0, z_\ell\}$ , see Figure 1) corresponding to a specific reflectivity measurement are then used to interpolate between entries in the  $\alpha_{ij}(p, T)$  tables in order to obtain  $\bar{\alpha}_{ij}^{(\ell)}$  appropriate to each atmospheric altitude level.

[20] Substituting equation (19) back into equation (16) and (17) yields

$$\hat{R}_{\text{surf}, j} = \Lambda \int_{-\infty}^{+\infty} \left\{ e^{-\sum_{k=1}^K \int_{z_0}^{\infty} \bar{\sigma}_k(z') n_k(z') \bar{\mu} dz'} \times \sum_i \frac{\sum_\ell \bar{\alpha}_{ij}^{(\ell)} N_\ell \bar{\mu}}{\sum_\ell N_\ell \bar{\mu}} e^{(-\xi_i \sum_\ell N_\ell \bar{\mu})} \frac{\delta\lambda}{\Delta\lambda_j} \right\} \times \mathcal{H}(\lambda, \lambda'; \Sigma) d\lambda' \quad (20)$$

$$\hat{R}_{\text{ss}, j} = \frac{p(\theta)}{4\mu_o} \int_{-\infty}^{+\infty} \left\{ \int_0^\infty \left[ \beta_{\text{sca}}(z, \lambda') \times e^{-\sum_{k=1}^K \int_z^\infty \bar{\sigma}_k(z') n_k(z') \bar{\mu} dz'} \times \sum_i \frac{\sum_\ell \bar{\alpha}_{ij}^{(\ell)} N_\ell \bar{\mu}}{\sum_\ell N_\ell \bar{\mu}} e^{(-\xi_i \sum_\ell N_\ell \bar{\mu})} \frac{\delta\lambda}{\Delta\lambda_j} \right] dz \right\} \times \mathcal{H}(\lambda, \lambda'; \Sigma) d\lambda' \quad (21)$$

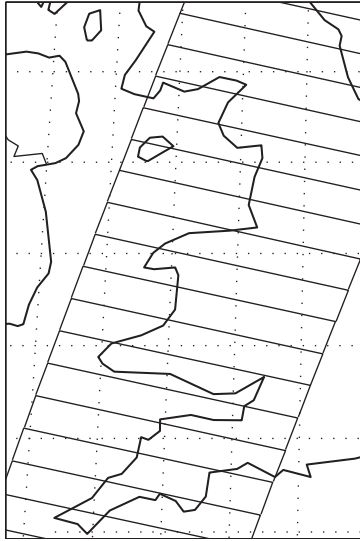


**Figure 2.** GOME ground surface pixel coverage (solid boxes) of about  $0.4^\circ \times 4^\circ$  shown along with the  $1^\circ$ -grid size of the ECMWF assimilation model (dotted grid).

which is the basic form used in this work for verification against forward modeling of the equations (14) and (15). We further include an additional first order polynomial term to account for the broadband contribution of aerosol scattering and multiply scattered photons, both for forward model verification against results from other radiative transfer models as well as in the retrieval algorithm (see section 7). The impact of the differential spectral contribution of this additional term is discussed in section 8.

## 4. GOME Measurements

### 4.1. Operation

[21] The GOME instrument is a four-channel grating spectrometer covering a wavelength range between 240 to 790 nm. The spectra are recorded simultaneously for each wavelength. The instantaneous nadir field of view (IFOV) is  $2.9^\circ \times 0.14^\circ$  (along  $\times$  across the track) and earth radiances are integrated for 1.5 seconds by scanning from east to west which corresponds to an earth footprint of about  $40 \times 320 \text{ km}^2$  (Figure 2). In the current study only nadir radiances are used so that the mean angle between the satellite IFOV and zenith is zero. However, we could easily account for other angles between the satellites line-of-sight and the zenith. GOME solar irradiance measurements are performed once a day. The detector pixel-to-pixel variability is smaller than 2% and is monitored by LED's illuminating the detector arrays. The correction for the pixel-to-pixel variability, the straylight and leakage fraction, and the noise produced by the cross-talk from the Peltier coolers is part of the level 0 to 1 data processing [Deutsches Zentrum für Luft- und Raumfahrt (DLR), 1996, 1999]. The solar irradiance and the earth radiance measurements are also corrected for the polarization sensitivity of the instrument. After applying these corrections the GOME level 1 data product provides a calibrated earth radiance spectrum  $I$  in photons ( $\text{cm}^2 \cdot \text{nm} \cdot \text{sec} \cdot \text{sr}$ ) and a calibrated sun irradiance spectrum  $\pi F$  in photons/( $\text{cm}^2 \cdot \text{nm} \cdot \text{sec}$ ). Table 2 summarizes some of the

most important instrument characteristics of the GOME instrument.

### 4.2. Spectral Resolution and Undersampling

[22] In a retrieval or in a study of forward modeled reflectivity using high resolution reference cross sections, a instrumental response function with a  $\sigma$ -width  $\Sigma$  has to be applied to the modeled reflectivity (equation (13)). This function takes into account the photon energy redistribution due to the slit. In the case of the GOME instrument it may be represented by convolving the radiatively transported absorption spectra with a Gaussian function which has a full-width-half-maximum (FWHM) of 0.27 nm. The detector pixel coverage is about 0.2 nm within channel 3, i.e. the convolved absorption spectrum is wavelength averaged over a wavelength region of 0.2 nm covered by each detector pixel. This means that in the case of GOME the spectral resolution ( $\Sigma$ ) is close to the spectral sampling by the detector pixels ( $\Delta\lambda$ ) and so the requirement that  $\Delta\lambda$  be much less than  $\Sigma$ , as was assumed for equations (16) and (17), is not satisfied, i.e. the instrument undersamples all absorption features with effective widths close to or smaller than the FWHM of the slit function.

### 4.3. Spectral Calibration and Rebinning

[23] The in-flight spectral wavelength calibration of the radiance and the irradiance is done using an on-board Pt/Cr/Ne hollow cathode gas-discharge lamp. Temperature changes over the orbit are taken into account in the spectral calibration. The error on the calibration is known to be on the order of 0.004 nm [Caspar and Chance, 1997]. We note that the interpolation of radiances measured by an instrument with a low sampling rate onto a different grid may introduce significant errors [Roscoe et al., 1996]. Moreover different wavelength calibrations are used for the sun irradiance measurement and the earth radiance. Thus, in this study, both spectra are rebinned instead of interpolated on a standard wavelength grid defined for an OACS retrieval. The rebinning procedure is carried out as follows. For each measurement, the GOME-reported radiance and irradiance wavelengths are assumed to define the central wavelengths of two different sets of bins. After adjustment for Doppler shift (see following paragraph), a fraction of the intensity within each bin is redistributed to the nearest bin of the predefined standard grid according to their fractional overlap in wavelength. In this way, the intensity of a high resolution reference absorption spectra integrated over one bin of the standard grid with  $\delta\lambda \ll \Delta\lambda$  can be correlated with the rebinned GOME detector pixel averaged intensity on the

**Table 2.** GOME Instrument Performance (585–600 nm)

	Value
Number of used detector pixels	69
FWHM slit function (ch3) <sup>a</sup>	0.27 nm
Detector pixel width $\Delta\lambda$ (ch3)	0.2 nm
Instantaneous Field Of View	$2.9^\circ \times 0.14^\circ$
Ground pixel size (Figure 2)	$40 \times 320 \text{ km}^2$
Pixel-to-pixel variability	<2%
Random noise value	0.1%
Accuracy of absolute radiances	1%

<sup>a</sup>Channel 3.

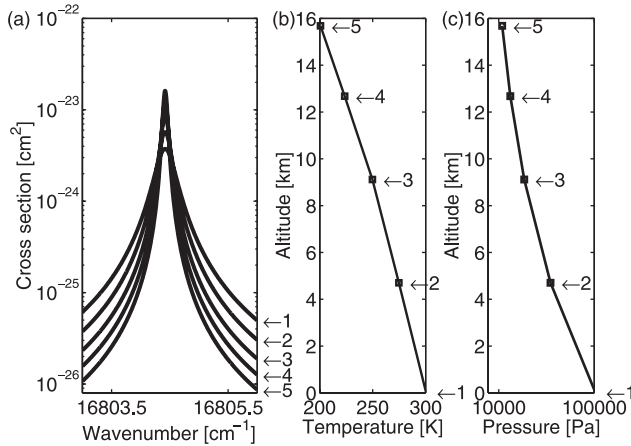


**Figure 3.** The effect on the shape of a water vapor absorption line at  $16804.42 \text{ cm}^{-1}$  in the earth's atmosphere due to the vertical change in temperature and pressure. The five line profiles in panel (a) correspond to five different altitudes taken from typical equatorial profiles of temperature (panel b) and pressure (panel c).

same grid without introducing errors in the integrated reflectivity per detector pixel bin. Thus, rather than adjusting the alpha coefficients for a shift of the wavelength grid due to different calibrations we adjust the measured GOME spectra to the standard grid used by OACS. The alpha coefficients can therefore be taken from a look-up table interpolated only over pressure and temperature (and not over wavelength).

[24] We correct the Doppler-shifted irradiance calibration with a knowledge of the relative velocity of the spacecraft to the sun provided for each sun irradiance measurement. The relative velocity is about 6 km/sec which results in a wavelength shift of about 0.01 nm (about 5% with respect to a pixel). Hereafter, reflectivity always refers to a Doppler shift-corrected measurement.

## 5. Molecular Absorption Spectra and Atmospheric Profiles

### 5.1. Water Vapor Absorption Spectra

[25] We use the HITRAN'96 database to calculate a number of realizations of a water vapor absorption spectrum covering the entire altitude range for which we have pressure and temperature profiles available, for each given geolocation. The main spectral parameters provided by the HITRAN'96 database are the integrated cross-section values (line strength)  $S_{\nu}$  in  $\text{cm}^{-1}/(\text{molec} \cdot \text{cm}^{-2})$  and the pressure-dependent air-broadened line half-width  $\gamma_{air}$  in  $\text{cm}^{-1}/\text{atm}$ . For a detailed description of the calculation of the temperature correction of the integrated line intensity the reader is referred to Rothman *et al.* [1998].

[26] The pressure-broadened line half-width-half-maximum HWHM  $\gamma(p, T)$  for a gas at pressure  $p_{air}$  [atm] and temperature  $T$  [K] is calculated by

$$\gamma(p, T) = \left(\frac{T}{T_{ref}}\right)^n (\gamma_{air}(p_{ref}, T_{ref})p_{air}), \quad (22)$$

where  $\gamma_{air}$  is the line-broadening contribution due to collisions with all other molecules, mainly nitrogen and oxygen, and  $n$  is the coefficient for the temperature dependence of the total line half-width [Rothman *et al.*, 1998].

[27] The largest expected volume mixing ratio of water vapor is of the order of  $10^{-2}$ . Therefore the self-broadening contribution is neglected in the calculation of the full-line half-width [cf. Liou, 1980]. Using a Doppler half-width, in  $\text{cm}^{-1}$ , given by  $\Delta_{\nu_D} = \bar{\nu}/c(\sqrt{2kT/M})$ , we calculate the wavenumber dependent cross-section in  $\text{cm}^2/\text{molec}$  using a Voigt line shape via

$$\sigma(\bar{\nu}, \bar{\nu}_0, p, T) = S_{\nu}(T)\Upsilon(\bar{\nu}, \bar{\nu}_0, p, T), \quad (23)$$

where  $\Upsilon$  is the normalized Voigt function in units of centimeters. The Voigt profile is numerically calculated using the algorithm by Armstrong [1967].

[28] Figure 3 shows an example of the change of the cross section due to the change in pressure and temperature over the dominant water vapor absorption altitude region from 0 to 16 km for one selected water vapor absorption line at  $16804.04 \text{ cm}^{-1}$ .

[29] The 590 nm water band is a ro-vibrational overtone band which is part of the  $5\nu$ -polyad (see Table 3). The band spans weak absorptions from about 565–605 nm. Due to an intensity mismatch of the GOME instrument resulting from spectral aliasing (P. Stammes, technical memo, 2000) between channel 3 and 4 we do not make any use of absorption lines above 600 nm. The lines below 585 nm are considered to be too weak and modeling of the background is complicated by a strong  $(\text{O}_2)_2$  absorption feature (see section 5.2 and Figure 5). The average lifetime of the excited ro-vibrational states is long enough for a collisional redistribution of the absorbed energy in the troposphere. Therefore the water vapor line shape is dominated by pressure broadening (Lorentz line shape) which introduces a significant change in the total transmitted light especially due to changes in the wings of the lines, where the cross-section may change over an order of magnitude over the first 16 km. Decreasing pressure and temperature gives rise to a significant decrease in the absorption. This effect may be different for two lines with overlapping wings, as is often the case for a typical water vapor spectrum.

[30] Following recent measurements of the cross-section of water vapor in the visible and near infrared evidence is growing for systematic deviations in the line-strength values from those given by the HITRAN'96 database [Carleer *et al.*, 1999; Belmiloud *et al.*, 2000; Learner *et al.*, 2000; Giver *et al.*, 1999]. We will discuss systematic

**Table 3.** Spectroscopic Values Relevant to the Water Vapor Band Under Study

	Value
WV-band ( $5\nu$ -polyad) wavelength range	585 – 600 nm
Other atmospheric constituents within above range	$(\text{O}_2)_2$ , $\text{O}_3$ , Na
Number of WV-lines (HITRAN'96)	638
HWHM WV-line $\gamma$	0.09 $[\text{cm}^{-1}]^a$
Grid size of reference spectra $\delta\lambda$	0.0117 $[\text{cm}^{-1}]$

<sup>a</sup> Average value within the WV-band at 1 atm.

patterns in the residuals between the results of our fits and the measured GOME spectra which we relate predominantly to errors in the values of the line parameters. A sense of the magnitude of the differences between such line-strength values coming from the database and the ones “measured” by the satellite instrument may be estimated for a specific radiative transport scenario. This estimate is based on residuals between forward models utilizing the HITRAN’96 line parameters and GOME measurements. The results are used to correct for differential fit mismatches (see section 10).

## 5.2. Other Sources of Extinction

[31] In this section other sources of extinction are discussed, which modify the reflectivity between 585 and 600 nm. These sources are Rayleigh scattering and scattering from aerosol loading as well as additional extinction by  $(\text{O}_2)_2$ ,  $\text{O}_3$ ,  $\text{NO}_2$ , sodium and the contribution of Fraunhofer line absorption. The fraction of photons generated by thermal emission is generally well below 1% and can therefore be neglected [Buchwitz *et al.*, 2000]. The Earth’s surface is treated as a wavelength-independent Lambertian reflector with albedo  $\Lambda$  diffusely reflecting a fraction of the light. Column density and cross-sections for the additional absorbers come from various independent sources and are used to model the total background correctly (Figure 4). This is necessary because modeling of the background using, for example, higher order polynomials may treat part of the low resolution water vapor spectrum as background and result in a lower retrieved WVC.

### 5.2.1. Rayleigh and Mie Scattering

[32] In order to calculate the total optical density, including the contribution of light scattered out of the light path (equation (14)) as well as the probability of scattering into the light path at each altitude  $z$  (equation (15)), we assume that Rayleigh scattering is the dominant scattering process. The Rayleigh scattering cross-section (equation (10)) in air is given by

$$\sigma_R \times 10^{24} = \frac{3.9993 \times 10^{-4} \nu^4}{1 - 1.069 \times 10^{-2} \nu^2 - 6.681 \times 10^{-5} \nu^4}, \quad (24)$$

where  $\nu = 1/\lambda$  [ $\mu\text{m}^{-1}$ ] and  $\sigma_R \times 10^{24}$  is given in units of  $\text{cm}^2$ , using the formulation of *Chance and Spurr* [1997]. The cross-sections are reproduced to better than 1% compared to the Rayleigh scattering cross sections tabulated by *Bates* [1984]. No attempt is made in this study to estimate the amount of scattering by large particles by means of Mie scattering. In this study we treat the contribution of Mie scattering (for example in clouds and from aerosols) to the total absorption as one of the major sources of error. We quantify the error from the influence of aerosol loading using a doubling-adding model which solves the equation of radiative transfer including all orders of scattering for both molecules and aerosols. The results are discussed in section 8.

### 5.2.2. Fraunhofer Line Absorption

[33] We estimated the effect of assuming a unstructured solar irradiance  $F_0$  using a high resolution sun spectrum from Kitt Peak ( $\Delta\nu = 0.02 \text{ cm}^{-1}$ ) [Wallace *et al.*, 1998] in

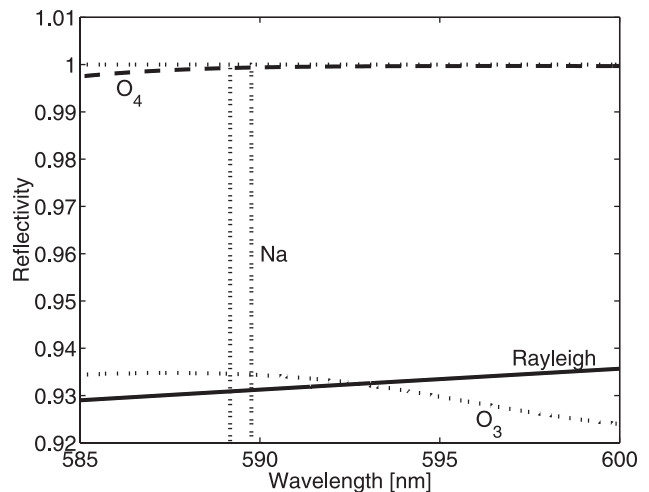


**Figure 4.** Construction of the background in the wavelength region between 585 and 600 nm.  $\text{O}_2$  and sodium densities are taken from two empirical atmospheric models [Hedin, 1991; Plane *et al.*, 1998]. The  $\text{O}_3$ -density is taken from GOME GDP level 2 data. Cross sections are taken from various sources described in the paper. The SZA is  $23^\circ$ .

the following way. We calculate the reflectivity including a sun spectra in equation (13) by

$$R_j = \frac{\pi}{\mu_0} \frac{\int_{\Delta\lambda_j} \int_{-\infty}^{+\infty} I(F_0) \mathcal{H}(\lambda, \lambda'; \Sigma) d\lambda' \frac{d\lambda}{\Delta\lambda_j}}{\int_{\Delta\lambda_j} \int_{-\infty}^{+\infty} F_0 \mathcal{H}(\lambda, \lambda'; \Sigma) d\lambda' \frac{d\lambda}{\Delta\lambda_j}}, \quad (25)$$

and compare it with the results of equations (14) and (15), where  $F_0$  in equation (25) is assumed to be constant and consequently divides out.

[34] The differences in reflectivity between including and excluding  $F_0$  have a maximum of 1% around the area of the sodium lines and less than 0.3% over the remaining wavelength range using the Kitt-Peak sun-spectrum together with a high WVC of  $1.44 \times 10^{23} \text{ molec/cm}^2$ . The assumption made for equations (14) and (15) therefore introduces a small, nevertheless not negligible, error in the area of the sodium absorptions (see also section 11.4).

### 5.2.3. Ring Effect

[35] The filling-in of Fraunhofer lines and atmospheric absorption structures due to inelastic rotational Raman scattering (Ring-effect) [Grainger and Ring, 1962; Chance and Spurr, 1997; Vountas *et al.*, 1998] usually needs to be considered in large parts of the GOME wavelength range, particularly in the ultraviolet. As mentioned in the previous section the region close to the sodium absorption may contribute somewhat to this effect. However, even though the wavelength region between 575 and 585 nm of GOME sun irradiance spectra exhibits similar or stronger Fraunhofer line structure than the region of the water vapor absorption, GOME reflectivity spectra (equation (13)) show only very weak structures within the former region. These structures can be related predominantly to the Ring effect because of the absence of other strong line

absorbers between 575 and 585 nm. It is therefore expected that also the Ring structures in the water absorption wavelength region is relatively small. In addition, accurate modeling of the Ring effect including polarization, which is needed for a polarization sensitive instrument such as GOME [Aben *et al.*, 2001], is very complicated and far beyond the scope of this paper. We therefore neglect the Ring effect for this study and discuss it as a possible source of error.

#### 5.2.4. Sodium

[36] In this work we model the contribution of the sodium background in the earth atmosphere at 588.9 and 589.5 nm to the total background absorption by calculating column concentrations for the non-sporadic atmospheric sodium layer at 90 km from a model by Plane *et al.* [1998]. Its contribution to the total sodium absorption with respect to the sodium Fraunhofer lines is very weak. A typical mean sodium column in the earth atmosphere is about  $6.9 \times 10^9$  molec/cm<sup>2</sup>. Nevertheless, it was found that modeling the sodium earth background absorption reduces the fit residual and improves convergence time. Thus, it is used in both forward modeling and the retrieval.

#### 5.2.5. (O<sub>2</sub>)<sub>2</sub> Collision Complex

[37] The atmospheric absorption feature of the (O<sub>2</sub>)<sub>2</sub>-collision complex within the region of 560 and 600 nm was investigated by Perner and Platt [1980]. Subsequently, Pfeilsticker *et al.* [1997] presented atmospheric measurements of (O<sub>2</sub>)<sub>2</sub> in the wavelength range from about 450 to 650 nm and Solomon *et al.* [1998] modeled and calculated the contribution of (O<sub>2</sub>)<sub>2</sub> to the total absorption in this region. Cross-sections of (O<sub>2</sub>)<sub>2</sub> have been measured by, for example, Greenblatt *et al.* [1990] and Newnham and Ballard [1998]. The cross-sections we use in this work are measured by means of Cavity Ring Down Spectroscopy by Naus and Ubachs [1999] for pressures between 0 and 1 atmospheres at room temperature. The results of both Greenblatt *et al.* and Naus and Ubachs indicate that we may safely assume negligible temperature dependence for the cross-section. The optical density is calculated for each ground pixel using an O<sub>2</sub>-density column from the Neutral Atmosphere Empirical Model MSISE90 [Hedin, 1991] for a given date, time, altitude-range and geolocation. Due to small variations in the O<sub>2</sub>-density the difference in densities in the slant path of the light with respect to the used vertical column densities from the Hedin model is small and may affect the results only for very high SZA. There is a significant absorption due to (O<sub>2</sub>)<sub>2</sub> visible in the GOME spectra on the blue side of our wavelength window for high SZA. Figure 5 shows such an absorption peak in the GOME spectra for the region between 560 and 600 nm at 62° latitude and for a SZA of 73°. For comparison we show a lbl forward calculation based on equations (14) and (15) including absorptions from (O<sub>2</sub>)<sub>2</sub>, O<sub>3</sub>, sodium and water vapor. The modeled spectrum is adjusted to the GOME measurement by fitting a first order polynomial to account for the unknown surface albedo  $\Lambda$  together with a first-order polynomial to account for the broadband contribution of aerosol loading and multiple scattering (equations (30) and (28)). Apart from the water window described in this study another water absorption at the blue side of the spectrum between 565 and 580 nm superimposed on the (O<sub>2</sub>)<sub>2</sub> absorption peak is clearly visible. The latter is

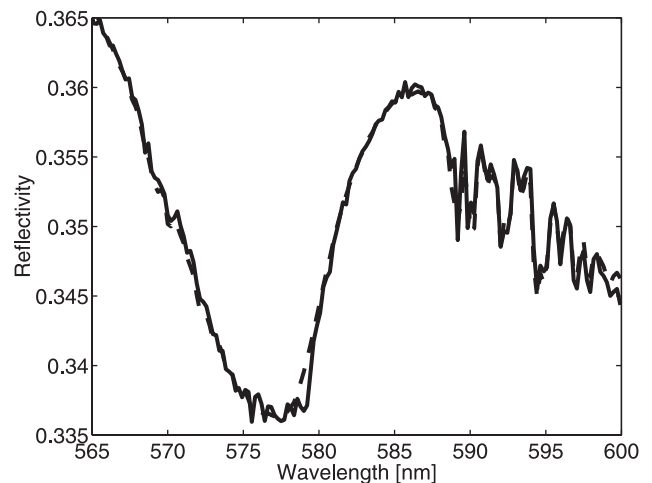


**Figure 5.** Comparison of a forward modeled lbl calculation (dashed curve) of the reflectivity using equations (14), (15) and (28) with a GOME measurement (solid curve) taken at 62°N (SZA = 73°). The background consists of (O<sub>2</sub>)<sub>2</sub>, O<sub>3</sub> and sodium. The stronger of the two (O<sub>2</sub>)<sub>2</sub> absorption peaks is clearly visible around 577 nm with another water vapor absorption band between 565 and 580 nm superimposed on it. In the case of the latter there are some discrepancies between model and measurement in the region between 575 and 580 nm which could be related to problems in the water vapor cross-section database.

reproduced well in the region between 565 and 575 nm, whereas the absorption features superimposed on the peak between 575 and 580 nm are poorly reproduced. This could be related to problems in the water vapor cross-section database.

#### 5.2.6. NO<sub>2</sub>

[38] Within our wavelength region of interest, NO<sub>2</sub> has an optical density of a maximum of  $1 \times 10^{-3}$  [Richter and Burrows, 2000] which is two to three orders of magnitude smaller than water vapor and about two orders smaller than the optical density of ozone. For the purpose of this paper and within the wavelength region used we neglect the contribution of NO<sub>2</sub> which is below the sensitivity limit of our method. Nevertheless small contributions of NO<sub>2</sub> absorption for high NO<sub>2</sub> content, for example in case of biomass burning, may contribute additional structure to our residuals.

#### 5.2.7. Ozone

[39] For the cross-section of the ozone Chappuis absorption band we use high-resolution reference spectra at atmospheric temperatures of 202, 221, 241, 273 and 293 K and pressures at 100 and 1000 mbar recorded using Fourier-Transform spectroscopy in the UV-visible-NIR spectral regions (240–850 nm) by Voigt *et al.* [2001]. The ozone slant column density (SCD) for a specific geolocation and SZA is taken from the GOME Data Processor (GDP) [Balzer and Loyola, 1996; DLR, 1999] level 2 data product [Burrows *et al.*, 1999]. Its accuracy is known to be on the order of 5% for SZA less than 70°. The optical density is calculated by integrating over the altitudes corresponding to the five cross section temperatures

listed above assuming the local pressure and temperature profile.

### 5.3. Pressure and Temperature Profiles

[40] The pressure and temperature profiles used in the retrieval are taken from ECMWF (compare section 5.1). The ECMWF data assimilation model [Vesperini, 1998] provides us with 31, 50 or 60 altitude levels in pressure and temperature, according as the date is before March 1999, after March 1999 and after October 1999 respectively. Data is provided for the entire globe at 0h, 6h, 12h, and 18h UTC with a ground pixel resolution of  $1^\circ$  in latitude and longitude. The data is interpolated onto a  $0.5^\circ$  grid that matches the resolution of SSM/I data and improves the overlap between ECMWF ground pixels and GOME ground pixel. GOME level 1 geolocation data consists of 5 data-tuples in latitude and longitude: 4 components for the edges and one for the center of a ground pixel. They span an area of roughly  $0.4^\circ \times 2.5^\circ$  in latitude and longitude (depending on the geolocation, see Figure 2). For each data-tuple the nearest ECMWF value is sorted out and a mean pressure and temperature is calculated for each altitude layer  $\ell$ . In this study we use up to 31 pressure and temperature levels which cover an altitude range between 0 and 23 km. The atmospheric layers  $\ell$  are defined as described in section 2. For each ground pixel a set of  $\alpha_j^{(\ell)}$  per detector pixel  $j$  for a given altitude layer  $\ell$  is calculated by interpolating alpha tables to the mean pressure and temperature (compare equation (30) and Figure 1) to be used in an OACS fast forward model or in an OACS fit to be described next.

## 6. Intrinsic OACS Accuracy

[41] The intrinsic accuracy of the OACS method is limited by two method-related sources of error: (1) the discretization error due to the Opacity Coefficient Method (OCM) caused by replacing the integrals in equations (16) and (17) (equations (20) and (21)); (2) exchange of the convolution with the sampling integral. This error is related to the fact that GOME detectors undersample the instrumental function of the instrument by  $\Delta\lambda \ll \Sigma$  (section 4.2). As mentioned in section 2 the first error may be reduced arbitrarily by decreasing  $\delta\lambda$  and thus increasing the number of realization points per absorption line of the high resolution reference spectrum. The second error, related to the basic transport equations (equations (14) and (15)), is introduced by performing the sampling of the high resolution reflectivity spectrum before the convolution (convolution problem), as is done for both equations (16), (17) and for the basic OACS equation (equations (20) and (21)). However, performing the sampling before the convolution makes the fitting much more efficient, because the convolution has to be performed only over 69 measurement points during each iteration step and not over the high-resolution absorption spectrum.

[42] In order to quantify the intrinsic method-related error we will compare the reflectivity calculated using the OACS method (equations (20) and (21)) with a lbl calculation based on equations (14) and (15). The density subcolumn profiles of water vapor per atmospheric level

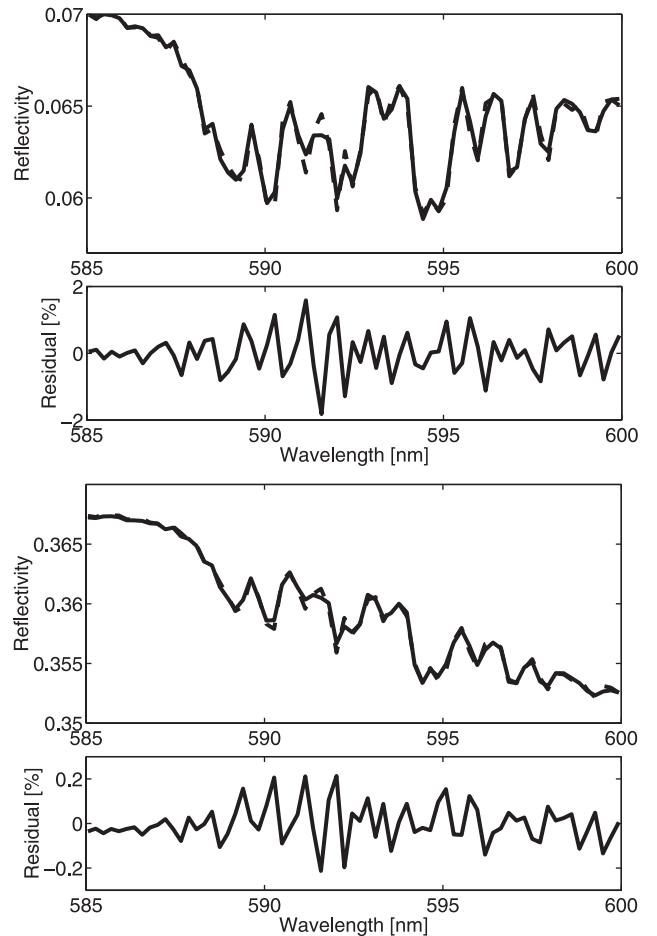


**Figure 6.** Comparison of modeled spectra for specific measurement scenes. The reflectivity plot shows a forward modeled lbl calculation using equations (14) and (15) (solid line) and a forward modeled reflectivity using the OACS method (equations (20) and (21); dashed line). The residual plot shows the relative method-related intrinsic error in reflectivity ( $|\text{lbl}-\text{OACS}|/\text{lbl}$ ; used throughout the paper). Upper two panels: A high WVC of  $1.34 \times 10^{23}$  molec/cm<sup>2</sup> measurement over the Pacific at  $23.5^\circ$  latitude and  $250^\circ$  longitude for a SZA of  $23.5^\circ$ . Lower two panels: A low WVC of  $8.19 \times 10^{21}$  molec/cm<sup>2</sup> for a measurement over land at  $62^\circ$  latitude and  $262.5^\circ$  longitude for a SZA of  $73^\circ$ .

for two specific geolocations are taken from the ECMWF data assimilation model. Figure 6 shows the comparison between both calculations for a typical equatorial scenario over the ocean with a high WVC of  $1.34 \times 10^{23}$  molec/cm<sup>2</sup> and a low WVC of  $8.19 \times 10^{21}$  molec/cm<sup>2</sup> over land at SZAs of  $23.5^\circ$  and  $73^\circ$ , respectively. Both ground pixels are cloud-free. The two figures also show the relative residuals between the lbl and the OACS forward model, which is defined as  $(\text{lbl}-\text{OACS})/\text{lbl}$ , hereafter. From the residuals we conclude that, for  $\delta\lambda = 2 \times 10^{-3}\Delta\lambda$ , the relative spectral accuracy of the method in reflectivity is better than 2% for high WVC and better than 0.2% for low WVC. For a comparison of reflectivities between the results of the lbl and the OACS forward model without performing the convolution the accuracy of the method

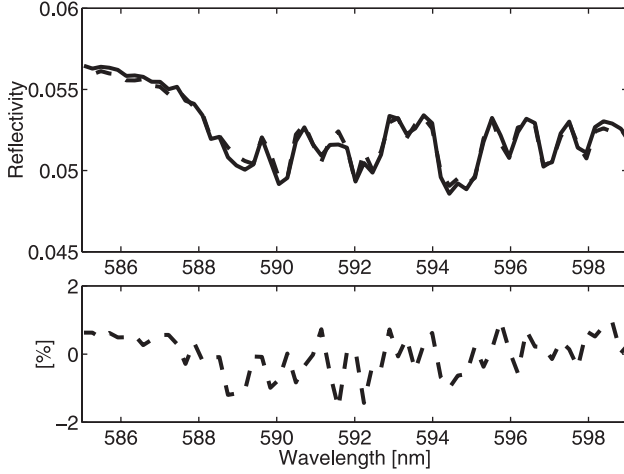


**Figure 7.** The upper panel shows a comparison between the results of OACS forward modeling (dashed line) and the doubling adding model (DAM, solid line) of *de Haan et al.* [1987]. A WVC of  $1.34 \times 10^{23}$  molec/cm<sup>2</sup> is assumed in the doubling adding code together with a SZA of 40°. The lower panel gives the relative residual.

appears to be better than 0.4% for high and better than 0.2% for low WVC. We conclude that the residual is dominated by error source number (2) above, namely the convolution problem.

## 7. Forward Model

[43] We use equations (20) and (21) to construct a basic fast forward model reflectivity spectrum which includes single-scattering via

$$R_j = \hat{R}(N_\ell, \Lambda_j; \tilde{\mu}_\ell)_{\text{surf},j} + \hat{R}(N_\ell; \tilde{\mu}_\ell)_{\text{ss},j}, \quad (26)$$

where  $j$  is the  $j$ th detector pixel within the window of interest. The altitude-dependent path length factor  $\tilde{\mu}_\ell$  is calculated using a Chapman function [*Banks and Kockarts, 1973*] which takes the curvature of the atmosphere into account. We adjust the forward modeled spectrum to the GOME measurement in the region between 585 and 600 nm by fitting a first-order polynomial for the unknown surface albedo  $\Lambda_j$ , assuming

$$\Lambda_j = A\lambda_j + B, \quad (27)$$

where  $A$  and  $B$  are free fit parameters. Since the differential contribution of multiple scattering and aerosol extinction appears to be lower than 2% in cases of cloud-free ground pixels (see section 8) within our spectral region of interest we include an additional first-order polynomial,

$$R_{\text{ms},j} = C\lambda_j + D, \quad (28)$$

where  $C$  and  $D$  are additional free fit parameters in order to account for the broadband contribution of higher orders of scattering.

[44] Thus, in its entirety, the forward model consists of three terms, viz.

$$R_j = \hat{R}(N_\ell, \Lambda_j; \tilde{\mu}_\ell)_{\text{surf},j} + \hat{R}(N_\ell; \tilde{\mu}_\ell)_{\text{ss},j} + R_{\text{ms},j}. \quad (29)$$

[45] Figure 7 shows a comparison between a solution of the full scalar radiative transfer equation using an independent method and the OACS forward model described above (equation (29)). For the full solution of the radiative transfer equation including the multiple scattering source term we use a doubling-adding model (DAM) [*de Haan et al., 1987*] (see also following section 8). The coefficients  $A$  to  $D$  used in equations (27) and (28) are retrieved by a fit to the solution of the DAM-model after the calculation of equations (20) and (21) is performed. We used a WV-subcolumn profile taken from the ECMWF assimilation model with a total WVC of  $1.34 \times 10^{23}$  molec/cm<sup>2</sup> under a SZA of 40°. For the DAM-model a maritime situation with a low surface albedo of 0.03 without aerosol loading is used. The comparison between the fast forward modeling using OACS and the full radiative transfer solution given by the DAM reveals a relative difference of less than 2% (Figure 7, lower panel) which is comparable to the intrinsic method-related accuracy of the method (see previous section). Note how there appears to be some degree of freedom left in the absolute quantities and spectral dependence of the usually unknown surface albedo as well as the broad-band multiple-scattering contribution. This is due to the fitting of the OACS forward model to the reference model spectrum (which is, in this case, the result of the DAM but will be, in the remainder of the paper, a small set of GOME measurements). Nevertheless, the surface albedo of 3%, as used in the DAM, is derived for the above case study to better than 35% at 592 nm (see Table 4). In future studies, this could be improved by replacing the first-order polynomial  $R_{\text{ms}}$  in equation (29) by an OACS-modi-

**Table 4.** Relative Contribution of Ground-Reflected, Singly Scattered and Multiply Scattered Photons to the Total Reflectivity Calculated by the DAM Model and for the Scenario Introduced in Figure 7<sup>a</sup>

	Model Input		Model Output			OACS Retrieval Results			
	AOD <sup>b</sup>	$\Lambda$	GR <sup>c</sup>	SS <sup>d</sup>	MS <sup>e</sup>	WVC ( $\times 10^{23}$ ), molec/cm <sup>2</sup>	$\Delta$ WVC, %	$\Lambda$	$\Delta\Lambda$ , %
Maritime clear sky	0	0.03	43.8	48.2	8.0	1.33	-7.7	0.040	+33.3
Maritime aerosol	0.21	0.03	20.0	53.2	26.8	1.65	+14.8	0.042	+40.0
Rural clear sky	0	0.10	69.1	22.8	8.1	1.42	-1.6	0.105	+5.0
Rural Aerosol	0.51	0.10	17.9	30.9	51.2	1.69	+17.6	0.109	+9.0

<sup>a</sup>DAM model calculations are performed assuming a SZA of 40° and a WVC of  $1.44 \times 10^{23}$  [molec/cm<sup>2</sup>] for each case.

<sup>b</sup>Aerosol optical depth.

<sup>c</sup>Percentage of ground reflected light at 592 nm.

<sup>d</sup>Percentage of single scattering at 592 nm.

<sup>e</sup>Percentage of multiple scattering at 592 nm.

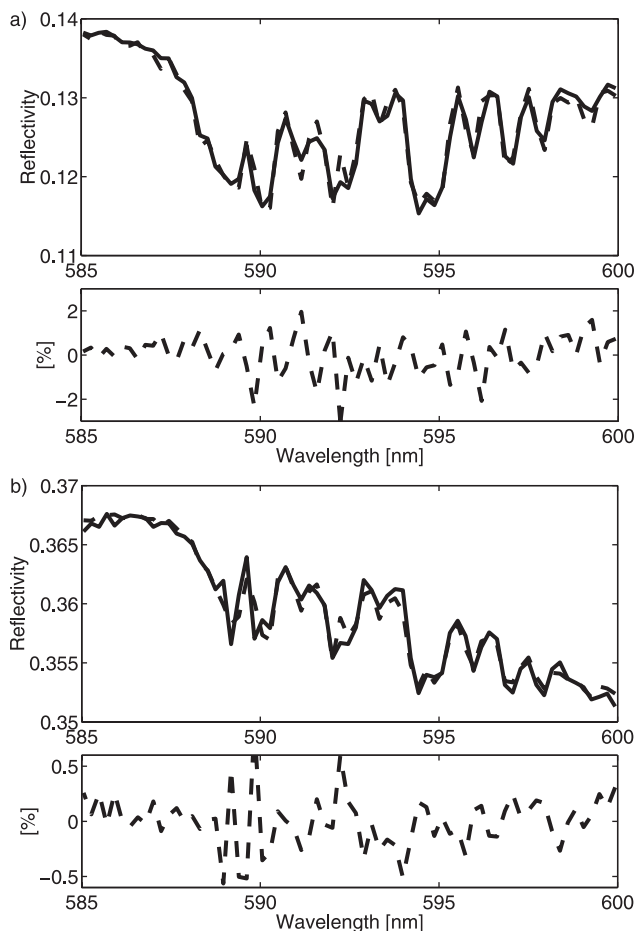


**Figure 8.** Forward modeling results from OACS (dashed lines) in comparison with GOME spectra (solid lines) taken at the same location. Temperature, pressure and water vapor concentration profiles have been taken from ECMWF. Upper two panels (a): Reflectivity spectra for a WVC of  $1.75 \times 10^{23}$  molec/cm<sup>2</sup> at a SZA of 27°. Lower panels (b): Same as upper panels but for a WVC of  $8.19 \times 10^{21}$  molec/cm<sup>2</sup> at a SZA of 73°. Both ground pixels are cloud-free. In both cases the lower plots show the residual. For the low WVC case (lowest panels) sodium line absorption in the region of 589.5 nm increases the residual significantly above the intrinsic method-related error value (compare Figure 6).

fied term which accounts for the differential contribution of higher-order scattering. In addition the surface albedo could also be retrieved from a fit to the spectrum in a spectral region beyond the water vapor absorption which may improve the robustness of the fit (see also section 11.5).

[46] A detailed description of the influence of different aerosol loading and the relative contribution of singly and multiply scattered photons on the reflectivity will be presented in the next section in which we also discuss the impact of aerosols and multiple scattering on the relative residuals between OACS and DAM.

[47] Figure 8 shows the results of a fast forward modeling of GOME spectra using equation (29) for a high and a low WVC. A total of 30 atmospheric layers  $\ell$  is used to cover altitudes up to about 23 km, with temperature, pressure and

water vapor subcolumn profiles taken from spatially and temporally collocated ECMWF data. The absorption due to other absorbers as well as the Rayleigh single scattering contribution are included as described in the previous section. Again, both residuals are on the order of the intrinsic method-related error for high and low WVC as shown in Figure 6. One exception is the wavelength region between 589 and 590 nm where the residual increases somewhat in case of low water vapor content.

## 8. Narrowband Contribution of Aerosol Loading and Multiple Scattering

[48] In the formulation of the basic transport equation (equation (9)) we neglect the contribution of multiply scattered photons to the total reflectivity. For the fast forward modeling as well as for the retrieval in the next sections we use a first order polynomial to account for the broadband multiple-scattering contribution (equation (28)). By this we neglect the narrowband (differential) contribution of water vapor to the total reflectivity caused by multiply scattered photons.

[49] To account for the full effect of multiple scattering, we solve the full scalar radiative transfer equation including the multiple scattering source term by employing the DAM, which, for our purposes, has been reduced to the scalar representation of the radiation field. The reflectance  $R(\lambda)$  is calculated in a line-by-line mode of a spectral resolution of  $0.01 \text{ cm}^{-1}$ . For the assessment of the effect of multiply scattered light on the measurement, we investigate four atmospheric scenarios: two with maritime and rural boundary layer aerosol loading and two clear-sky scenarios (i.e. without aerosols). All scenarios include the effects of Rayleigh scattering, ozone absorption and (maritime or rural) Lambertian ground-level reflection. In the case of the maritime scene we use a surface albedo of 3% whereas for the rural scene a surface albedo of 10% is used. For maritime aerosol loading a constant particle density of 4 000 particles per cm<sup>3</sup> is assumed. For the middle and upper troposphere, we assume a tropospheric background aerosol, for which the particle density decreases with the third power in pressure. The optical properties of the aerosols are taken from *Shettle and Fenn* [1979]. The total aerosol optical depth is 0.26 at  $\lambda = 590 \text{ nm}$ . In the rural case we have chosen a constant but much higher particle density of 15 000 particles per cm<sup>3</sup> below 1 km and the total aerosol optical depth is then 0.51 at  $\lambda = 590 \text{ nm}$ .

[50] Table 4 lists the relative contribution of ground-reflected, singly and multiply scattered photons as a percentage of the total reflectivity using the DAM-model for four different aerosol loading cases as described above. Without aerosols the maximum contribution of multiply scattered photons is below 10% in the wavelength range between 585 and 600 nm. Single scattering is the dominant source of reflectivity (50% effect) in the maritime aerosol scenario because of low surface albedo and the ground-reflected component is comparable to that due to multiple scattering. This may be contrasted with the rural aerosol scenario in which multiple scattering is the dominant source of scattered light (50%) due to the high aerosol optical density. Aerosols reduce the ground-reflected component by up to 20–50%.

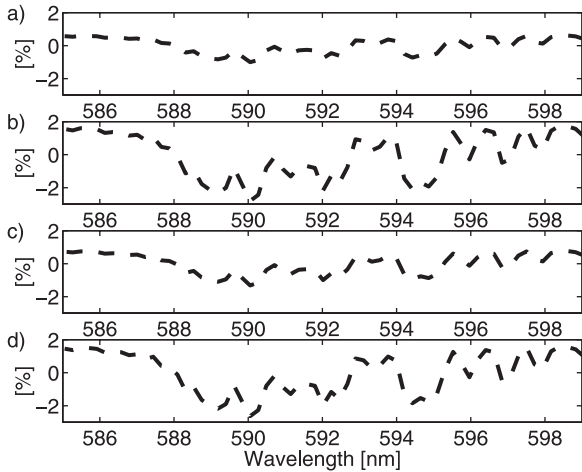


**Figure 9.** Relative differences between the lbl model presented in this paper based on equations (14), (15) and (28) and the result of the DAM for the specific scenario presented in Figure 7. The upper two panels show the results for a maritime case with a surface albedo of 3% under (a) clear sky conditions and (b) with maritime aerosol loading. The lower two panels show the results for a rural case with surface albedo of 10% for (c) clear sky conditions and (d) with rural aerosol loading.

[51] In addition to the evidently broadband aerosol effects just discussed it is also reasonable to expect that a significant differential contribution due to multiply scattered photons may affect the retrieved WVC. Since the radiation transport model presented in this paper does not explicitly account for the latter we present a comparison in Figure 9 between a lbl calculation based on equations (14), (15) and (28) and the results of the DAM forward model for the four scenarios discussed above. The parameters C and D needed for the lbl calculation are obtained by a fit to the DAM result. The differences in the residuals between Figures 9a and 9c and Figures 9b and 9d indicate that aerosol-loaded scenarios may give rise to significant differential structure. The latter is a 2% effect compared with a 20–25% broadband aerosol contribution. Even though this is comparable to or just below the 2% precision of the OACS method for high WVC it is a systematic effect. In section 9.4 we therefore perform OACS retrieval on all four spectra modeled by the DAM in order to estimate the effect of multiple scattering due to Rayleigh and aerosol scattering on the retrieved WVC together with the effect of aerosol extinction.

## 9. Sensitivity Analysis of the Retrieval Method

### 9.1. Retrieval Method

[52] We fit equation (29) to GOME reflectivity spectra along with optical densities of  $O_3$ ,  $(O_2)_2$  and sodium as well as the Rayleigh scattering contribution as described in section 5. The numerical method used is a robust, non-linear, large-scale trust-region method [Byrd *et al.*, 1988] which solves the optimization problem

$$\min_{N_\ell, \Lambda_j, R_{ms,j}} \sum_j \left[ R_j - \left( \hat{R}(N_\ell, \Lambda_j; \tilde{\mu}_\ell)_{\text{surf},j} + \hat{R}(N_\ell; \tilde{\mu}_\ell)_{\text{ss},j} + R_{ms,j} \right) \right]^2. \quad (30)$$

[53] The fit parameters are the vertical water vapor column densities  $N_\ell$  of  $\ell$  atmospheric layers and the surface albedo and multiple scattering parameters (see section 7). All 69 measurement points  $j$  within our region of interest are fitted simultaneously together with the four parameters A to D.

[54] For each OACS fit we start with a flat water vapor sub-column profile  $N_{\ell,0} = 10^{16}$ , where the  $N_\ell$  are given in units of the water vapor vertical column density per atmospheric layer (compare equation (19)). Each fit is constrained by an upper limit  $N_{\ell,max}$  in the form of a step function with high values over the first atmospheric layers and lower values for the higher levels. The lower profile constraint is set to  $N_{\ell,lower} = 0$ . The constraints prevent the fit from giving too much weight to the higher altitude levels which otherwise would increase the relative contribution of the single scattered photons and, in so doing, decrease the total mean free path length. The latter would lead to a reduced total WVC. The effect of introducing this constraint is to reproduce the relative single-scattering contribution to the total reflectivity to better than 1% when compared to the results given by the lbl forward model.

### 9.2. Precision and Accuracy of the Fitting Method

[55] We henceforth adopt the term precision to describe measurement-related random errors and the term accuracy to describe the absolute difference between the true and the retrieved value due to systematic errors. These differences are caused by the response of the result due to the intrinsic method-related error as well as the robustness of the result to errors in the main input quantities: the accuracy of the measurement and the altitudes profiles of atmospheric temperature and pressure. The random noise of a typical satellite measurement is dependent on photon shot noise, detector shot noise and digitization effects and is quantified to be about 0.1% of the absolute radiance in the case of GOME [DLR, 1999]. The GOME instrument is also sensitive to the polarization of the light which is measured for each channel. In what follows we adopt a total system error for GOME measurements of about 1%. This is derived from a full error calculation including random noise errors, the error of the fractional polarization values, the polarization correction factor and the error on the instrument response function known from pre-flight calibration studies. As mentioned in section 4.3 the error on the spectral calibration is known to be on the order of 0.001 nm within our wavelength region [Caspar and Chance, 1997]. For the temperature and pressure profiles taken from the ECMWF data assimilation model an uncertainty of 0.3% [Filiberti *et al.*, 1998] in pressure and 0.1% in temperature [Francis and Schweiger, 2000] is assumed.

[56] We estimate precisions and accuracies for the retrieval of WVCs using OACS (equation (30)) from the lbl forward modeled spectrum used before to estimate the intrinsic method-related error (section 6, Figure 6) as follows. One hundred simulated reflectivity spectra are produced by adding random noise errors normally distributed around one third of the reflectivity values, randomly chosen, where the  $2\sigma$  range is given by their random noise values provided with the measurement. The noise values are taken from level 1 data for both solar irradiance and earth radiance. At the same time and for each modified spectrum the wavelength grid is

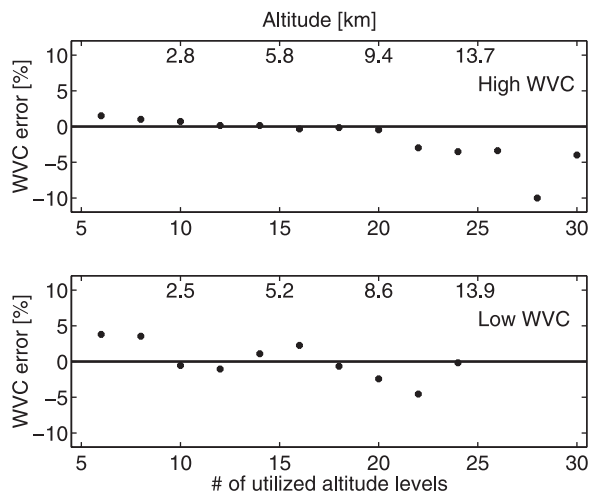


**Figure 10.** Relative residuals of the retrieved WVC (dots) from lbl forward modeled spectra using the OACS method. Typical examples are given for a high WVC (upper panel) of  $1.34 \times 10^{23}$  molec/cm<sup>2</sup> and a low WVC (lower panel) of  $8.19 \times 10^{21}$  molec/cm<sup>2</sup> covering different altitude ranges as follows. Each value  $x$  on the abscissa represents the utilization of  $\ell = 1$  to  $x$  atmospheric layers in the retrieval. Best results were achieved when using about 18 altitude levels (covering the range of 0 to 10 km). For the low WVC the fit fails to converge within the given limits when utilizing more than 24 levels.

shifted randomly within the calibration error range in order to simulate calibration errors. In a separate calculation we shift the temperature and pressure profiles used in the fit to their expected maximum and minimum values due to potential systematic errors in the ECMWF database. In the same simulations we similarly increase and decrease the reflectivity by 1% in order to explore the effects of the systematic uncertainties in the measured intensities. This permits a check of the precision (standard deviation for the mean retrieved WVC from artificial spectra with random noise added), the accuracy (mean retrieved WVC for the random noise modified spectra) and the robustness or total accuracy (response to shifted input profiles and known systematic errors in the measurements) of the method.

### 9.3. Sensitivity Study Results

[57] Figure 10 shows two representative examples of OACS WVC fit results for two artificial modified spectra utilizing different altitude ranges for a fixed density sub-column profile with a relatively high WVC of  $1.34 \times 10^{23}$  molec/cm<sup>2</sup>. Each fit covers a range of atmospheric levels between 0 and the value denoted on the x-axis. Each atmospheric level is defined as described in section 3 and shown in Figure 1. In general, best results are obtained with an altitude range covering 18 atmospheric levels (corresponding to a range of about 10 km above the earth surface) with the full range of WVCs agreeing to better than 2%. This altitude range is sufficient to cover the bulk of the water vapor at any geolocation while still keeping the number of fit parameters as small as possible (the water density drops by more than two orders of magnitude over the first 10 km, see WV-subcolumn profile in Figure 11).

For higher altitude ranges there is not sufficient information to restrict the fit. These findings are supported by the calculation of mean weighting functions

$$\partial R^{(\ell)} / \partial n_{VC}^{(\ell)} \Big|_j$$

per atmospheric layer and per detector pixel  $j$  (Figure 11), where  $R$  is the OACS formulation of the reflectivity based on equation (29). Up to the 18th altitude level the weighting functions show similar changes in the reflectivity per altitude level with respect to changes in the water vapor density  $n$  (Figure 1). Above about the 20th level small changes in the water vapor density induce large unsystematic changes in the reflectivity for different wavelengths. This results in additional local fit minima which makes the fit unstable and increases the uncertainties in the fit results (see retrieved WVC results in Figure 10 using more than 20 atmospheric layers). For the retrieval of WVCs presented in this paper we therefore utilize 18 atmospheric levels to achieve best results for the full range of very high and very low WVCs.

[58] Figure 12 shows retrieved WVCs from 100 forward modeled, random noise-modified spectra. Two extreme cases are considered: a high WVC ( $1.34 \times 10^{23}$  molec/cm<sup>2</sup>) and a low WVC ( $8.19 \times 10^{21}$  molec/cm<sup>2</sup>). First, we performed 100 OACS fits to the modified spectra using exactly the same pressure and temperature profiles as used in the forward model. The precision of the method is given

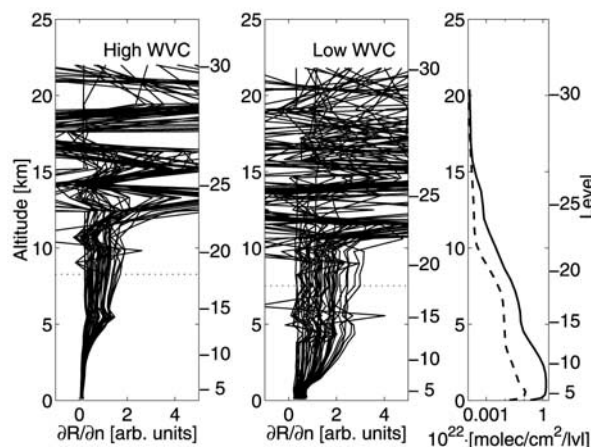


**Figure 11.** Change in reflectivity due to change in water vapor density over altitude (weighting functions  $\partial R / \partial n$ ) for the forward modeled reflectivity over altitude using OACS. The left panel shows the result for the high WVC and the middle panel for the low WVC used in Figure 10. Each plot consists of 69 weighting functions, one for each GOME detector pixel in the wavelength range between 585 and 600 nm. The dotted line denotes the maximum (18th) atmospheric level (right axes) used in the retrieval. For comparison the panel on the right shows the corresponding water vapor subcolumn profile for the low (dashed line) and the high WVC (solid line). Above the 18th level small changes in the water vapor density introduce large changes in the reflectivity value.

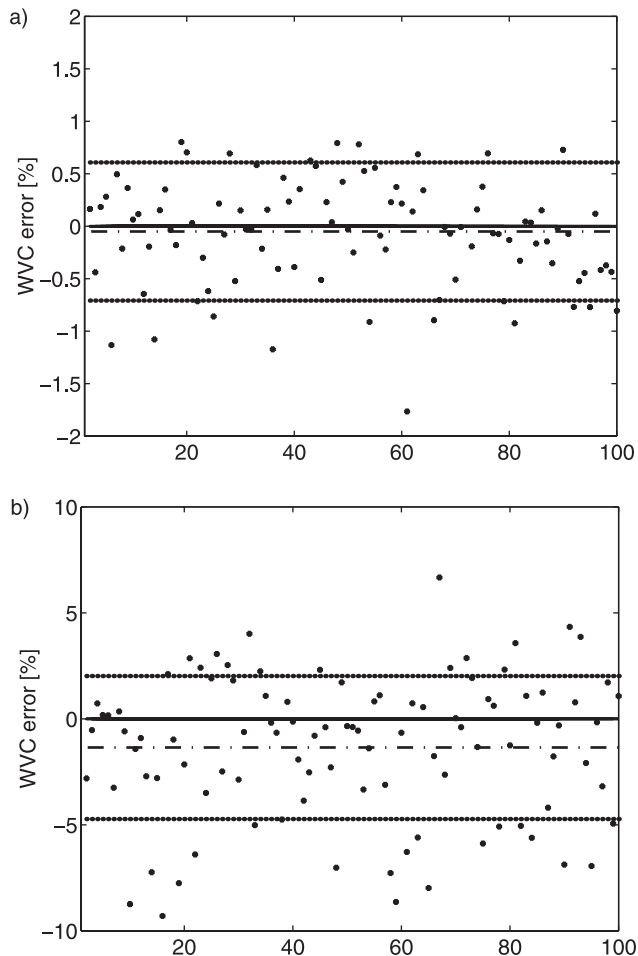


**Figure 12.** Relative differences (dots) between the OACS-retrieved WVC and the WVC used for 100 lbl forward modeled spectra. The forward modeled spectra are modified by expected instrument random noise and calibration errors for the high and low WVC cases used in Figure 10 (upper panel (a) and lower panel (b), respectively). The  $1\sigma$  standard deviation (dotted lines) is 0.66% for high WVC and 3.4% for low WVC. The difference between the mean of the 100 retrieved WVCs and the input WVC is given by the dotted-dashed line. From this we estimate an accuracy for the method of 0.05% for high WVC (a) and 1.35% for low WVC (b).

by the  $1\sigma$ -distribution of the resulting values around their mean value. In the case of high WVC the precision is 0.66% and for low WVC it is 3.4%. The difference between the mean value and the WVC value used as an input in the model provides the accuracy of the method which is 0.05% for high and 1.35% for low WVCs. In both cases OACS underestimates the WVC used in the lbl model. Second, 100 fits to the random noise modified spectra are performed with shifted input profiles and spectral intensities. All possible combinations in the shifted inputs (shifted to the lowest and highest expected values within their range of uncertainty) are taken into account. The maximum impact on the WVC for all the possible cases reveals a total accuracy of the method due to changes in the input profiles of at most 0.8 and 4% for high and low columns, respec-

tively, which we interpret as the robustness of the method to systematic errors in the input quantities.

#### 9.4. Impact of Multiple Scattering and Aerosol Loading on the Retrieved WVC

[59] We performed OACS retrieval on all four spectra modeled by the DAM and described in detail in section 8. The results listed in Table 4 reveal a very small error for cases with no aerosol loading and surface albedo of 10% and an error of at most 18% for high aerosol loading with an optical depth of 0.51. We get an error of  $-7\%$  in the case of a maritime situation without aerosol loading, where the contribution of multiple scattering is relatively weak (8%). This is because the retrieval of such a small surface albedo ( $+30\%$  error) is difficult to achieve in conjunction with the fit parameters of a broadband multiple scattering contribution. An overestimated surface albedo leads to an overestimation of the ground reflected light contribution and therefore to an underestimation of the WVC. The maritime retrieval results in Table 4 show that the effect of multiple Rayleigh scattering and surface albedo retrieval ( $-7\%$  error on the WVC) together with aerosol loading ( $+14\%$  error) may often cancel out for intermediate aerosol loading. This cancellation may not occur for rural cases where significant aerosol loading and increased multiple scattering may lead to an overestimation of the WVC in all the cases. In general, an increased aerosol loading leads to an enhanced multiple scattering contribution and therefore to longer light-paths than expected by the model. The latter results consequently in an overestimation of the WVC.

[60] In summary we conclude that the inclusion of an additional polynomial (equation (29)) seems to be an adequate approach to treat the broad-band multiple scattering and aerosol contribution to the reflectivity. We thus expect an error of at most 18% on the retrieved WVC due to differential contributions of multiple scattering and aerosol loading in extreme cases. The systematic errors due to the differential contribution especially in cases of high aerosol loading remains a subject for future study.

## 10. Retrieval From GOME Data

[61] We performed OACS fits for a single GOME track on October 23, 1998, between  $-80^\circ$  and  $80^\circ$  in latitude for a series of longitudes between  $117^\circ$  and  $279^\circ$  for 470 measurements. As mentioned earlier, a step function is used to constrain the fit by an upper limit for each value  $N_1$  (section 9.2). The shape of the step function is scaled with respect to an expected WVC such as can be taken from climatology. In our case we scale the upper profile constraint differently for geolocations with high ( $>1 \times 10^{23}$  molec/cm<sup>2</sup>), medium (between  $1 \times 10^{23}$  molec/cm<sup>2</sup> and  $1 \times 10^{22}$  molec/cm<sup>2</sup>) and low ( $<1 \times 10^{22}$  molec/cm<sup>2</sup>) expected WVC. The climatology is derived from ECMWF. The convergence tolerance limits are set to  $1 \times 10^{11}$  molec/cm<sup>2</sup> for the WVC value and  $1 \times 10^{-11}$  for the optimization function values. The fit has converged when one of the tolerance limits is reached.

### 10.1. Differential Fit Mismatches

[62] The upper panel of Figure 13 shows the mean value of 250 residuals of OACS fits for cloud-free ground pixels over the described GOME track. All these residuals display

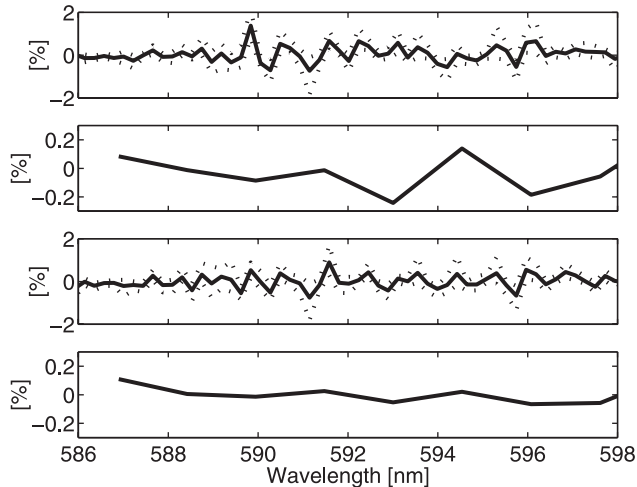


**Figure 13.** A cumulative plot of 250 OACS fit residuals of cloud-free ground pixels for a GOME track on October 23, 2000 between  $-80^{\circ}$  and  $+80^{\circ}$  in latitude. The upper panel shows the mean value and outer limits of all residuals for OACS fits without any correction applied. The second panel shows the mean value of a moving average applied over 8 detector pixels. Note the different scale with respect to the first panel. The third panel shows the residuals in the corrected cases applying equation (33). We use only one calculation of  $\Delta\phi$ , i.e. from one geolocation, for all fits. The lowest panel shows the moving average over 8 pixels applied to the residuals after corrected fitting.

similar spectral patterns which are related to the spectral pattern of the intrinsic method error residual shown in Figure 6. This high frequency pattern has a rate of  $0.8 \text{ nm}^{-1}$  which corresponds to a half-cycle of 4 detector pixels each of which covers a region of  $0.2 \text{ nm}$ . The second panel shows a moving average of the mean residual values over 8 detector pixels, i.e. over two cycles of the intrinsic error residual. The result is a clear averaging out of the high frequency structure. However in the region between 591 and 597 nm a lower frequency structure contained within the residuals does not vanish. We relate this low frequency differential fit mismatch predominantly to instrumental errors as well as systematic deviations in the line strength values given by the HITRAN'96 database used in this study. However, other systematic errors introduced by the measurement or the modeling of the background may also contribute to this effect (see end of next section and discussion in section 11.4).

[63] In November 1999 new measurements of the water vapor absorption lines lying both within the 590 nm band as well as in other bands were published [Giver *et al.*, 1999] which showed relative differences in the integrated line intensities with respect to the values given by HITRAN'96 of up to 17%. However measurements of water vapor absorption bands other than the one used in this study [Learner *et al.*, 2000] recently showed discrepancies ranging from about 100% for small lines to about 20% for strong lines for the main water vapor absorption bands in the region between 1110 and 685 nm. They also found systematic differences in various bands ranging from 6% to 33%. Even though measurements by Learner *et al.* in the wavelength

range between 585 and 600 nm have not intensively been studied yet large differences in some of the water absorption bands between 1110 and 685 nm suggest the presence of potentially large uncertainties in the reference cross sections of the HITRAN'96 database used in this study. In addition, the measurements by Giver *et al.* correct the line intensities in many cases to lower values whereas in the measurements of Learner *et al.* predominantly higher values were found [Belmiloud *et al.*, 2000]. Measurements of the water vapor absorption bands by Carleer *et al.* [1999] and results of Cavity Ring Down measurements performed by Naus *et al.* [2001] also show significant differences from HITRAN'96 in the absorption line strengths within the 590 nm band. This suggests that systematic database errors may contribute significantly to the observed differential fit mismatch.

## 10.2. Adjustment for Errors in Input Quantities

[64] In order to describe a mismatch in the  $j$ th pixel between the model and the measurement we define a parameter  $\phi$  as follows. Assume that  $R_{mod}(\phi)_j$  is the top-of-the-atmosphere reflectivity calculated by a lbl forward model using the values from a specific spectral database, i.e.  $R_{mod}(\phi_0)_j$  is the modeled reflectivity before applying any spectral database correction. The modeled reflectivity should properly include all physical effects such as background scattering or other absorptions as well as a convolution integral and pixel-binning to simulate the instrument sampling. It is further assumed that there exists some  $\Delta\phi$ , i.e. a small correction to the parameter  $\phi$ , which may be applied to the modeled reflectivity  $R_{mod}(\phi_0)_j$  in order to reproduce the measured satellite reflectivity  $R_{sat}_j$ ,

$$\phi_0 \rightarrow \phi_0 + \Delta\phi = \phi \quad (31)$$

$$R_{mod}(\phi_0)_j \rightarrow R_{mod}(\phi)_j = R_{sat}_j. \quad (32)$$

Without loss of generality it is possible to represent the general model reflectivity  $R_{mod}(\phi)_j$  as an exponent of a function  $f$  containing  $\phi$ , so that

$$R_{sat}(\phi)_j = e^{f(\phi)} \approx R_{mod}(\phi_0)_j \exp\left(\left.\frac{\partial f}{\partial \phi}\right|_{\phi=\phi_0} \Delta\phi\right), \quad (33)$$

Here  $f$  has been expanded in a Taylor series to first order assuming a linear response to errors in  $\phi$ . Thus equation (33) allows direct estimation of  $\Delta\phi$  directly from measurements and models of those measurements, assuming that the models are correct. equation (33) is also used in the retrieval presented in this paper to correct for the systematic differential fit mismatches showed in Figure 13.

[65] It is possible to show empirically that  $\Delta\phi$  is a robust quantity with respect to the geometry of the measurement (i.e. it is independent of the geolocation) when  $\partial f / \partial \phi|_{\phi=\phi_0}$  is identified with effective optical density of a pixel  $\hat{\tau}$ . In order to do so, we calculate  $\Delta\phi$  using equation (33) for three different GOME measurements  $R_{sat}$  in the equatorial, the sub tropics and polar region, i.e. for a high, mean and low water column (Figure 14). In each case a lbl forward model  $R_M$  was used based on equations (14) and (15) including a fit to the surface albedo  $\Lambda$  and the broadband multiple scattering contribution using equations (27) and (28) respectively. For the forward modeling we use water vapor subcolumn profiles

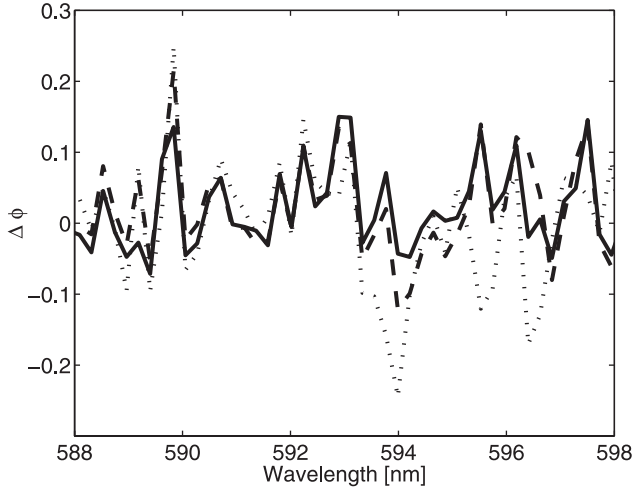


**Figure 14.** Pixel-to-pixel variation of  $\Delta\phi$  calculated for three different GOME measurements. In each case the GOME measurement is used together with the corresponding lbl forward model result to calculate  $\Delta\phi$  from equation (33). Values of  $\Delta\phi$  for a high (solid), medium (dashed) and a low WVC (dotted line) are shown. The measurements were taken at significantly different geolocations with SZAs of  $37^\circ$ ,  $23^\circ$ ,  $73^\circ$ , respectively. The three curves show similar spectral patterns which are quite different from the absorption signature of water vapor (compare Figure 13). Below 588 and above 598 nm the differences between the modeled and measured spectra are small and the results are dominated by the noise of the measurement.

from the ECMWF database where the total column densities differ less than 5% from the SSM/I value. Two important error sources have to be taken into account: (1), the assumption on the water subcolumn profile made by using the ECMWF water vapor values and (2), the contribution of differential residual pattern due to narrowband multiple scattering effects which may both affect the spectral shape of the curves. However, the effect of both of these errors should be seen in the spectral dependence of the derived  $\Delta\phi$  (Figure 14) as they both would display the characteristic absorption pattern of the water vapor lines. In contrast to this the derived  $\Delta\phi$  in Figure 14 does not show this characteristic pattern for all three scenarios. The figure also shows that the spectral dependence of  $\Delta\phi$  exhibits a similar shape in all cases in the region of strong water absorption between 587 and 598 nm which is independent of the geometry of the light path.

[66] Uncertainty in spectral database information might be summed up as arising either out of missing line data or errors in existing line parameters. *Belmiloud et al.* [2000] showed that for water vapor the effect of erroneous line intensities was probably greater than the effect of missing lines, at least in the case of HITRAN'96 which is the database used for our retrieval. Thus in what follows we assume that the relative error in the cross-section of a pixel is dominated by the relative error in the pixel-averaged line intensity,

$$\frac{\Delta\hat{\sigma}}{\hat{\sigma}} = \frac{\Delta\hat{S}_v}{\hat{S}_v}, \quad (34)$$

where  $\hat{S}_v$  represents a pixel-averaged line intensity (compare equation (23)). It is also assumed that the effect on the line

intensity of different temperatures for different light paths is small.

[67] In order to link the  $\Delta\phi$  correction, which we relate to the differential fit mismatch, to uncertainties in line intensities of the gas in question we consider the following.

[68] Assume that effective cross-sections  $\hat{\sigma}_{sat,j}(s)$  and  $\hat{\sigma}_{mod,j}(s)$  exist which satisfy

$$R_{sat}]_j = \exp\left(-\int_s \hat{\sigma}_{sat,j}(s)n(s)ds\right), \quad (35)$$

$$R_{mod}]_j = \exp\left(-\int_s \hat{\sigma}_{mod,j}(s)n(s)ds\right). \quad (36)$$

[69] Then setting  $\hat{\sigma}_{sat,j}(s) - \hat{\sigma}_{mod,j}(s) = \Delta\hat{\sigma}$  and  $\hat{\sigma}_{mod,j} = \hat{\sigma}$  in equation (34) we obtain

$$\begin{aligned} R_{sat}]_j &= R_{mod}]_j \times \exp\left(-\int_s [\hat{\sigma}_{sat,j}(s) - \hat{\sigma}_{mod,j}(s)]n(s)ds\right), \\ &= R_{mod}]_j \times \exp\left(-\frac{\Delta\hat{S}_{v,j}}{\hat{S}_{v,j}} \int_s \hat{\sigma}_{mod,j}(s)n(s)ds\right). \end{aligned} \quad (37)$$

[70] If  $\partial f/\partial\phi|_{\phi=\phi_0}$  from equation (33) is identified with the optical density in equation (37) then  $\Delta\phi_j = -\Delta\hat{S}_{v,j}/\hat{S}_{v,j}$  is a quantity which depends purely on errors in pixel-averaged line strength. It represents the correction required to bring the cross-section using the line strength values of the spectral database into agreement with what the real cross section should be, given the correct atmospheric profile and the assumptions listed above.

[71] The third panel in Figure 13 shows the same mean residual as in the upper most panel but now for fits where the correction (equation (33)) is applied using only one calculation of the differential fit mismatch  $\Delta\phi$  for a single geolocation. For these fits the low frequency pattern in the region between 591 and 597 nm vanishes when applying the moving average over eight detector pixels (lowest panel). The derived WVCs are changing by applying the correction to values which are on average 17% higher than the values received from the uncorrected fits. Based on the assumption of a non-scattering atmosphere and relating the differential fit mismatch  $\Delta\phi_j$  solely to systematic errors in the cross-section, we estimate the error in the pixel-averaged line strength  $\Delta\hat{S}_v/\hat{S}_v$  (equation (37)) to be on the order of 10 to 20%. Apart from these errors in the line strength values of the spectral database, additional systematic contributions to the differential fit mismatch can be instrumental errors or the structures in the sun irradiance spectrum due to Fraunhofer line absorption. The latter is estimated to contribute less than 15% to the value of the differential fit mismatch in the region of the sodium lines and less than 5% to the remaining wavelength region based on the calculations explained under 5.2 using equation (25) with and without a constant  $F_0$  together with equation (33).

### 10.3. Corrected Retrieval Results

[72] Figure 15 shows OACS WVC fit results which include the line-strength correction for the same track as

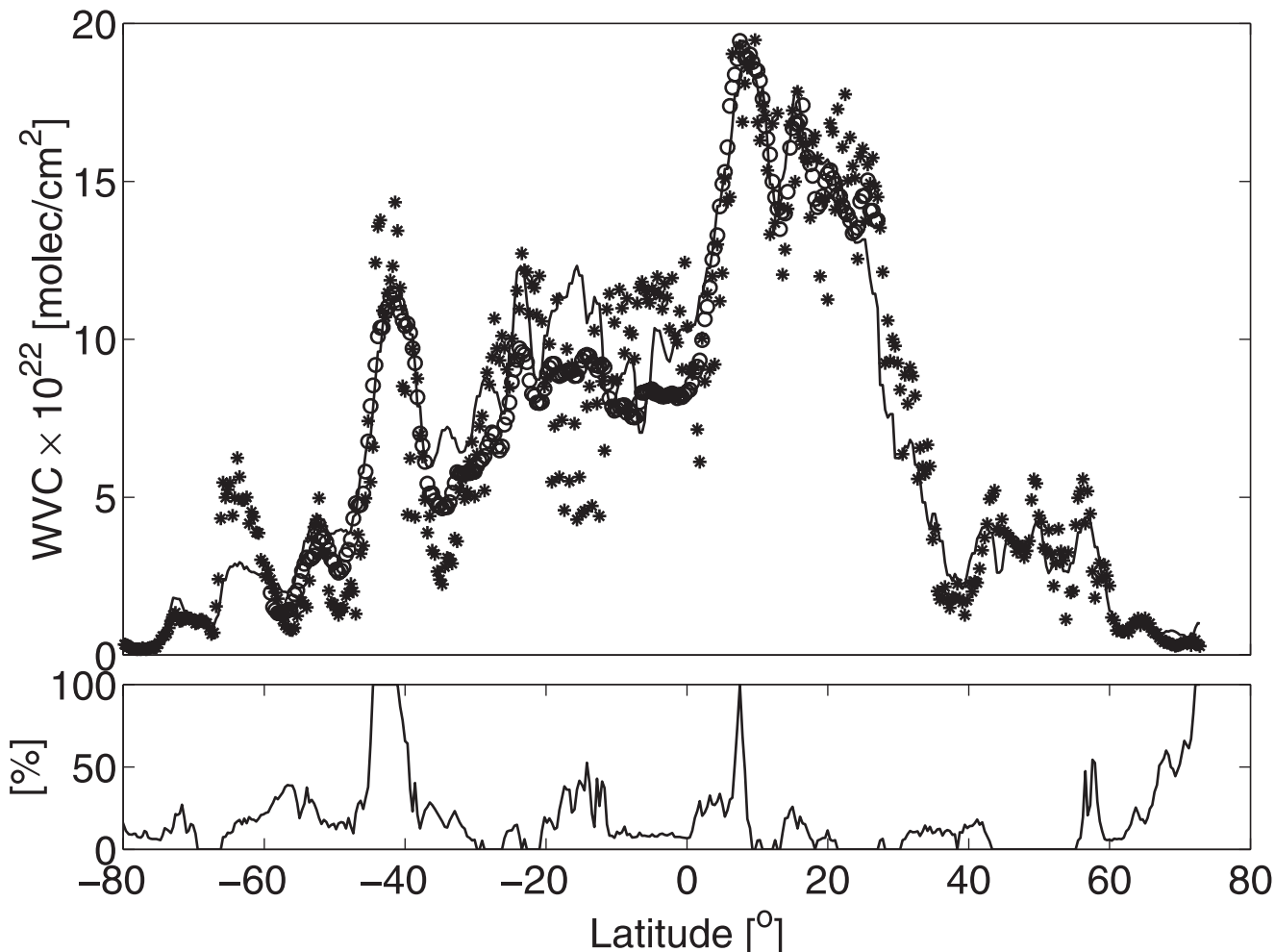


**Figure 15.** OACS WVC fit results over latitude (upper panel, stars) for a GOME track on October 23, 1998 covering longitudes from 117°E at 73° latitude to 279°E at -80° latitude. By way of a preliminary validation we also show the values given by ECMWF at 18:00 UTC (solid curve) and the SSM/I Microwave Sounder between 15:49 UTC and 16:39 UTC (circles). SSM/I data is not available over land (>30° latitude). The cloud coverage in percentage per ground pixel is taken from GOME GDP level-2 data and is indicated by the solid curve in the lower panel. OACS-retrieved WVCs decrease in the case of strong cloud coverage e.g. at 8° and -18° in latitude.

described in section 10.2. For comparison we show the WVC values as given by the ECMWF data assimilation model and the SSM/I microwave sounder which forms part of the Defense Meteorological Satellite Program (DMSP) F14 satellite platform. SSM/I global swath data are averaged on a  $0.5 \times 0.5$  degree global grid. Data from descending swathes are used in order to reach maximum overlap with the corresponding GOME track. We average the data from each GOME ground pixel within a range of, on average,  $4^\circ$  in longitude and  $0.4^\circ$  in latitude for each of the GOME geolocation 5-tuples of the GOME ground pixel (see also section 5.3 and Figure 2). SSM/I data is not available over land. The percentage cloud cover, also shown in the figure, is reported by GDP level-2 data. OACS fits give good results for GOME ground pixels with low cloud cover using the first 18 pressure and temperature levels from the corresponding ECMWF pressure and temperature profiles. In addition, the dynamic range in the WVC

densities ranging from values of  $8 \times 10^{20}$  molec/cm<sup>2</sup> in the polar regions to values of about  $1.5 \times 10^{23}$  molec/cm<sup>2</sup> at the equator is well reproduced and the variation between successive ground pixels is very low.

[73] The response of the retrieval method to the presence of high cloud cover does not always result in a drop in WVC as might be expected for clouds that block the light from traveling through the lower troposphere where the bulk of the water vapor is located. The latter is the case, for example, in the region around  $-18^\circ$ , where the retrieved columns are significantly smaller than the values given by ECMWF and SSM/I. This also applies to the narrow feature with strong cloud cover at  $8^\circ$  latitude for which OACS retrieves lower WVC than is retrieved from the surrounding ground pixels. The same is the case for the somewhat broader cloud cover at around  $-42^\circ$ , even though the drop over about six ground pixels is surrounded by higher WVC.

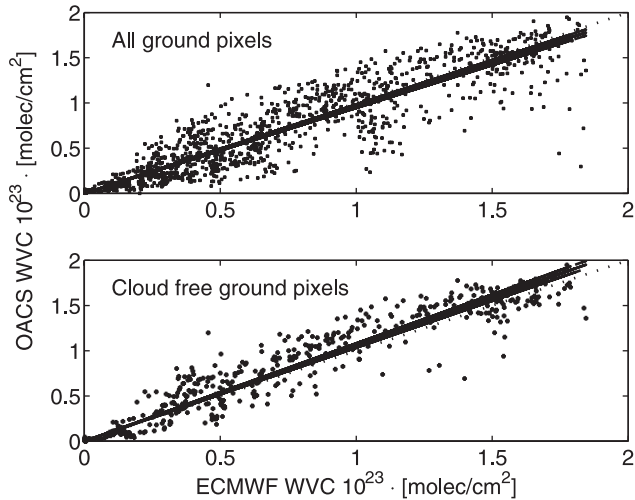


**Figure 16.** The two panels show scatter plots for WVCs retrieved by OACS in comparison with those given by ECMWF for all retrieved ground pixels (upper panel) and for ground pixels where the percentage cloud coverage is less than 10% (lower panel). OACS WVCs are retrieved for three different GOME tracks between  $-80^\circ$  and  $+80^\circ$  in latitude: on February 25, 1997 from 11:26 to 12:01 UTC at longitudes ranging from  $322^\circ E$  to  $322^\circ E$ , on September 30, 1999 from 0:09 to 1:05 UTC between  $82^\circ E$  and  $213^\circ E$  longitude and on October 23, 1998 from 17:52 to 18:32 UTC between  $117.16^\circ E$  and  $278.82^\circ E$  longitude. ECMWF data is given for 12:00 UTC and 00:00 UTC and 18:00 UTC respectively. The solid lines in both panels denotes the best fit of a linear polynomial through the OACS WVC values with the 99% confidence interval for each residual surrounding it. The gradients are 0.96 for all pixels and 1.06 for the cloud-free pixels.

[74] There are no regions to be found where OACS systematically under- or overestimates the values given by ECMWF or SSM/I over a large area. Most of the systematic differences over broader latitudinal regions are related to the presence of clouds.

[75] OACS retrievals of WVCs including the line-strength correction were performed on two additional GOME tracks. One track occurred on February 25, 1997 from 11:26 to 12:01 UTC at longitudes ranging from  $322^\circ E$  to  $322^\circ E$  and another on September 30, 1999 from 0:09 to 1:05 UTC covering longitudes from  $82^\circ E$  to  $213^\circ E$ . ECMWF data is given for 12:00 UTC and 00:00 UTC respectively. These GOME tracks were chosen predominantly for their good temporal and spatial overlap with SSM/I data and their relatively low cloud content. Figure 16 shows a scatter plot comparing OACS-retrieved and ECMWF WVCs for all ground pixels (upper panel) and separately for cloud-free pixels where the percentage cloud coverage is less than 10% (lower panel) including all three GOME tracks. The scatter between OACS WVC values and values of ECMWF for all three tracks is smaller than 50% and the systematic deviation is small. The gradient of the linear fit through the results is 1.06 in the cloud-free case (lower panel, Figure 16). The average effect on the retrieved column due to the presence of cloud is a drop in the WVC,

which results in a gradient of 0.96 for all examined ground pixels (upper panel, Figure 16). Figure 17 shows four scatter plots for cloud-free pixels for three different ranges of SZAs as well as for pixels over the ocean (low surface albedo) only. The results show that OACS is stable to changes in the surface albedo as well as to the geometry of the measurement.

[76] Figure 18 shows two typical line strength-corrected OACS fits for geolocations with high and low water vapor content together with their residuals. Both residuals are comparable to or smaller than the intrinsic method-related error and show essentially random scatter except for the region of strong sodium absorption in cases where the water vapor content is low (Figure 18b).

## 11. Discussion of Results

[77] Thus far a number of assumptions have been made with respect to the treatment of the radiative transfer problem, the modeling of the background absorption and the quality of the input and reference data. The aim of this section is to discuss the preliminary validation of the OACS WVC results in light of known systematic differences between ECMWF and SSM/I and the influence of clouds and surface albedo.

### 11.1. Summary of Results

[78] The results presented in section results and displayed in Figure 16 show that the correlation between the OACS-GOME results and the reference ECMWF/SSM values is very good. The absolute differences between ECMWF data and OACS retrieved WVC can be bigger than 50% for some cases, whereas the mean scatter is better than 11% for ground pixels with no cloud cover and better than 30%

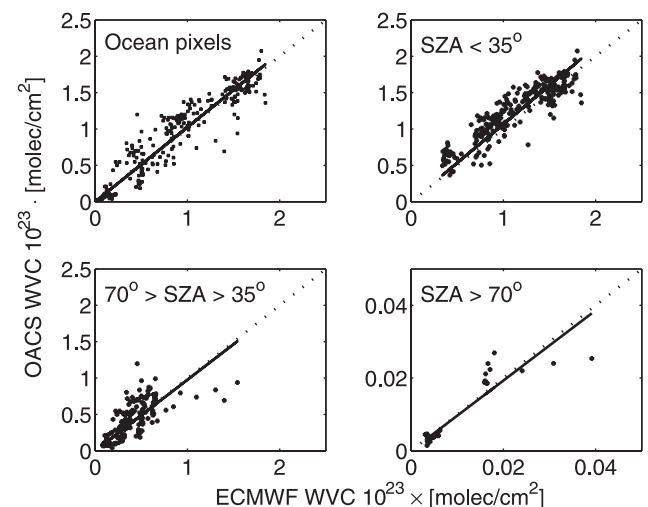


**Figure 17.** The four panels show scatter plots of WVCs retrieved by OACS from GOME measurements of cloud-free ground pixels in comparison with the values given by the ECMWF data-assimilation model. All studied GOME tracks described in Figure 16 are included. The upper left panel gives results for measurements over the ocean only, i.e. with a low surface albedo. The other panels give results for different SZA ranging between  $20^\circ$  and  $85^\circ$ .

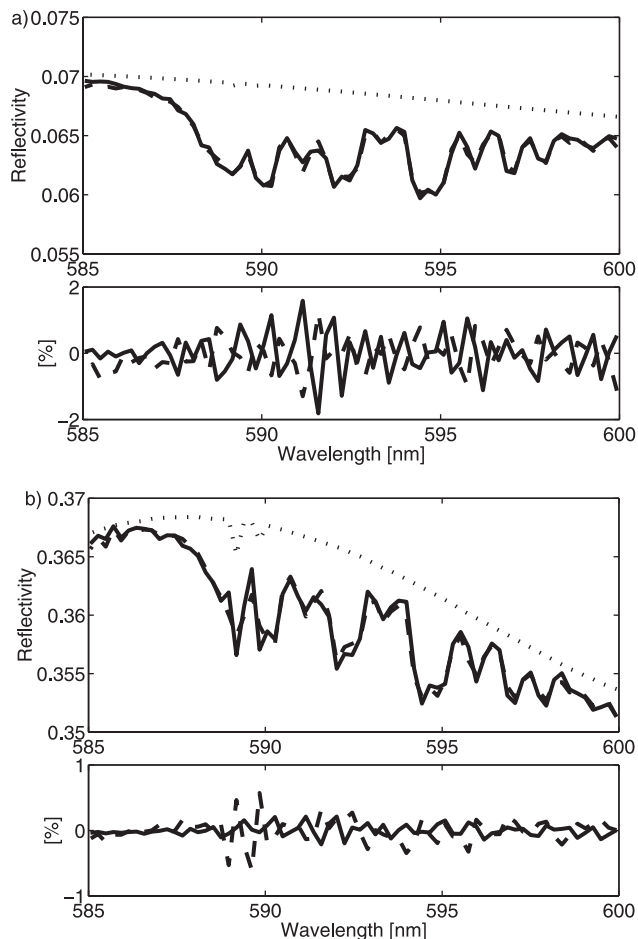


**Figure 18.** Results and residuals of typical OACS fits to two cloud-free GOME measurements for the case of high WVC (panels a) and low WVC (panels b). The solid lines in the both of the upper panels represent the GOME reflectivity. Dashed lines in the upper panels represent the OACS fit. The background (all absorbers other than water vapor) is shown by the dotted lines. The residuals (dashed lines) are compared, in both of the lower panels, with the intrinsic method related error (solid lines; compare Figure 6).

for all retrieved ground pixels. The method-related sensitivity and accuracy is of course significantly better.

### 11.2. Validation Data Sets

[79] In general, comparisons between WVCs given by ECMWF and SSM/I show significant discrepancies. ECMWF is known to underestimate WVC values given by SSM/I by 30–50% in the tropics and to overestimate in the sub-tropics by as much as 60% depending on season and geolocation [Vesperini, 1998]. ECMWF WVC values over the ocean are predominantly based on data from the TIROS N operational vertical sounder (TOVS). The standard deviation between TOVS WVC and radiosonde data in the 1000–850 hPa layer is known to be on the order of 20% and less than 40% in the layer between 500 and 300 hPa [Chaboureaud et al., 1998].

[80] The temporal and spatial collocation of GOME data with validation data is a significant challenge in its own

right. All GOME measurements may be temporally collocated to within one hour of ECMWF values. Nevertheless, changes in the water vapor densities within this time window are possible. Such changes may contribute to both the scattering and the systematic effects in a comparison between the two data sets. As is shown in Figure 2 the spatial overlap between the GOME ground pixel size and the smoothed ECMWF data gives rise to a higher spatial sensitivity of the OACS results in the latitudinal direction, whereas in longitudinal direction the spatial resolution of ECMWF data is significantly better. However, the change in water vapor column density over longitude is expected to be much lower than in the latitudinal direction [Randel et al., 1996; Vesperini, 1998].

[81] It was noted before that OACS-retrieved WVCs do not show any significant systematic differences from the values given by ECMWF. Small overestimations of the OACS WVCs with respect to ECMWF values can be examined for SZA smaller than  $35^\circ$  including the tropical region (Figure 17, upper right panel). A small fraction of WVCs retrieved for cloud-free pixels and SZA between  $35^\circ$  and  $70^\circ$  (including the sub-tropical region) exhibit smaller values than given by ECMWF (Figure 17, lower left panel). From this we conclude that OACS-retrieved WVCs from the GOME tracks used in this study are consistent with the trends observed from an intercomparison between ECMWF and SSM/I. For higher SZA above  $70^\circ$  (lower right panel) there is no clear effect on the retrieved column of an enhanced contribution of multiply scattered photons. However, the number of retrieved pixels is too small for good statistics.

### 11.3. Clouds

[82] Systematic deviations of the WVCs from the values of ECMWF appear to be related predominantly to the presence of clouds. Clouds may affect the retrieved WVC in two ways. On the one hand, light may be blocked by clouds from traveling through the lower troposphere where the bulk of the water vapor column is situated. This would cause a drop in the retrieved WVC. On the other hand, an enhanced path length due to multiple scattering in the clouds might yield an increase in the retrieved WVC. Therefore the result of the net effect will depend on cloud top height, the cloud character and the thickness of the cloud layer. As described in section results we found that strong cloud cover often causes a decrease in the retrieved WVC (Figure 16). However, in some cases the opposite effect occurs. In general, the good correlation between ECMWF and OACS as well as the relatively small response to the presence of clouds suggests that the effect of the blocking of the light and the effect of enhanced path length may often compensate each other.

[83] The cloud cover fraction is reported by GDP level-2 data. This fraction is derived by the initial cloud fitting algorithm (ICFA) and cloud top pressure is taken from the International Satellite Cloud Climatology project (ISCCP) [Koelemeijer and Stammes, 1999]. Differences in the retrieved cloud fractions with respect to the collocated Along Track Scanning Radiometer-2 (ATSR-2) can be as much as 0.18 [Koelemeijer and Stammes, 1999]. We call a GOME ground pixel cloud-free when the ICFA algorithm reports a cloud fraction of lower than 0.1. Therefore, large parts of the scattering in the case we call cloud-free (Figure 16) may be

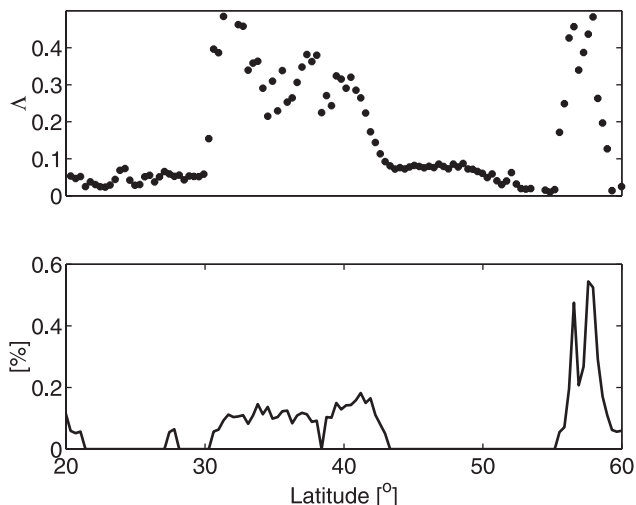


**Figure 19.** Surface albedo  $\Lambda$  at 590 nm retrieved with the OACS method for the GOME track described in Figures 15 (upper panel). The first part of the track (which covers 40° to 60° latitude at about 260° in longitude) starts over the Canadian Shield which is dominated by water in the form of lakes and by vegetation. OACS retrieved albedos between 0.03 and 0.1 for cloud free pixels (the percentage cloud cover is shown in the lower panel). The other part, from the Rocky Mountains over the Gulf of California and the Pacific (40° to 20° latitude at about 255° in longitude), frequently yielded albedos below 0.05.

attributed to ground pixels partially covered by clouds or errors in the cloud fraction values given by GDP level-2 data.

#### 11.4. Differential Fit Mismatch

[84] For the calculation of the error  $\Delta\phi$  of the model input parameter  $\phi$  we assumed that the water vapor sub-column profile concentrations used in the calculation of  $R_M$  given by ECMWF are close to reality. We further assumed that the differential contribution of multiple scattered photons are weak. The signatures of both of these errors, not to mention some contribution of the Ring effect and the Fraunhofer line effect discussed in sections 5.2 and 10.2 especially in the two pixels covering the sodium lines, should also contribute to the differential spectral structure of the calculated cross-section correction  $\Delta\phi$ . We quantified the contribution of the Fraunhofer line effect to be less than 15% of  $\Delta\phi$  in the area around the sodium lines and less than 5% in the remaining wavelength region. The signature of neglecting the differential impact of multiple scattering in the calculation of  $\Delta\phi$  should be visible as a systematic effect (compare section 8 and Figure 9) displaying the differential structure of the water vapor absorption. This effect is extremely small. Consequently, we relate the differential fit mismatch predominantly to instrumental pixel-to-pixel variations which are not corrected for by the level 1 data processing together with errors in the line strength databases. This places an upper limit of accuracy on the latter of about 10 to 20%.

#### 11.5. Surface Albedo

[85] For each OACS fit we retrieve a surface albedo  $\Lambda$  (equation (27)) assuming that the surface may be modeled

as a Lambertian reflector. Figure 19 shows the retrieved albedo at 590 nm together with the cloud cover for the same GOME track shown and described in Figure 15. The cloud-free results are comparable with those of *Koelmeyer et al.* [1997] using GOME measurements with an atmospheric correction scheme. However, the wavelength dependence of the albedo (equation (27)) within our spectral window might be influenced by the simultaneously fitted multiple scattering term (equation (28)). A fit to the solution of the DAM revealed an albedo accuracy of about 30% at 592 nm for a ocean type surface albedo of 0.03 (Table 4). For higher albedo over land (around 0.1) the accuracy is better than 10% due to the model calculations and retrievals. The impact of multiple scattering and aerosol extinction can introduce errors in the retrieved albedo value of up to 40% for maritime cases. The response to clouds is also clearly visible in Figure 19. In the case of strong cloud cover the retrieved albedo can easily reach 0.5.

## 12. Overview and Outlook

### 12.1. Summary

[86] We have shown that OACS is able to forward model upwelling reflectivity with accuracies better than 2%, when compared to results from a lbl calculation. In column retrieval terms, the precision of OACS (which depends on instrumental characteristics) is 0.66% for high WVC and 3.4% for low WVC. The accuracy of the method is better than 0.05% and 1.4% for high and low WVC, respectively. Besides calibrated radiances, the only necessary inputs from an operational perspective are specific temperature and pressure profiles for a given geolocation and SCDs of ozone. Method inputs which are pre-calculated and stored in lookup tables include pdfs of water vapor cross-section realizations taken from the HITRAN'96 database and cross-sections of  $(O_2)_2$  and  $O_3$ . The robustness or total accuracy of the method due to errors in the input pressure and temperature profile was found to be between 0.8% and 4% for high and low WVC, respectively. The obtained WVCs for cloud-free ground pixel situations correlate very well to WVCs given by ECMWF and SSM/I. The ground pixel-to-pixel variation of the retrieved column densities are low and the method is robust to changes in surface albedo as well as changes in the SZA.

### 12.2. Implementation and Routine Retrieval

[87] We have introduced, tested and presented a preliminary validation of a novel, fast forward modeling and retrieval method. The intention was to develop a relatively fast method for modeling spectral measurements for which the instrumental resolution is much broader than the absorption features of the trace gas under study. OACS uses a pdf coefficient method for the calculation of reflectivities containing the full altitude-dependent structure of the spectrum which can be stored in a look-up table. OACS forward modeling is very fast with respect to line-by-line methods and a retrieval of trace gas column from constituents with narrowband absorption spectra can be done on reasonable time scales. A retrieval of WVCs as described in this paper utilizing 18 altitude levels takes about 20 minutes per measurement on a Pentium II, 450 MHz, using an uncom-

piled MatLab code. Although this is still slow with respect to recent other DOAS methods [Buchwitz *et al.*, 2000; Noël *et al.*, 1999] fitting time can be improved significantly by porting the algorithm to a compiled language and using improved computer power. For the purpose of faster but less comprehensive on-line retrieval preliminary testing indicates that accuracies in the total retrieved WVC comparable to OACS can be obtained by replacing the basic exponential sums with a spectral structure parameterization-modified DOAS formulation (DOAS-SSP) [Maurellis *et al.*, 2000b] which is approximately twenty times faster than OACS and considerably easier to implement in a routine retrieval context.

### 12.3. Future Developments

[88] Improvements in the accuracy of the results and the stability of the fit may be gained by using additional information about surface albedo, cloud cover and cloud height. For example, surface albedo may be obtained by inspection of the region beyond the edges of the water vapor absorption band. Using such additional inputs would reduce the parameter space in the fitting of WV-subcolumn profiles and thus reduce the freedom of the fit in giving too much weight to the atmospheric scattering contribution by reducing the surface albedo or vice versa. The current OACS modified solution of the radiative transfer equation is best applied only to ground reflected and single scattered photons. We have shown that this is sufficient for retrieval of WVC from operational GOME data, utilizing the spectral water vapor window between 585 and 600 nm, within an accuracy of 18%, which is comparable to or better than available operational data products. In future studies the first-order polynomial accounting for the broad-band absorption contribution of multiple-scattered photons in the fast forward modeling as well as in the retrieval might be replaced by a full OACS-modified solution for higher orders of scattering. This could also serve as a starting point for implementing aerosol scattering and absorption parameters. However, OACS could be easily applied in its current form to measurements of the water vapor absorption in the infrared regions around 2  $\mu\text{m}$  of the forthcoming SCIAMACHY instrument on the ENVISAT platform, where the contribution of multiple scattering is much smaller than in the visible region.

### 12.4. Conclusions

[89] Apart from the application to routine trace gas retrieval OACS provides an efficient tool for studying physical processes from remote-sensing spectral measurement. This is because OACS is based on a fundamental, physical model. Consequently, it may be used to validate laboratory measurements of trace gas absorption cross-sections with measurements from satellites. For example, we have shown that there is some evidence for inaccuracies in the HITRAN'96 database as proposed by recent measurements of the water vapor absorption line parameters. Additionally, the fast forward modeling capabilities of OACS can be used to model and study atmospheric absorption features other than water vapor, as we demonstrated in case of the  $(\text{O}_2)_2$  absorption feature around 575 nm even for high SZA. A future application of OACS in the near infrared will be to forward model water vapor absorption bands in

spectral regions containing absorption features of atmospheric species other than water vapor.

[90] **Acknowledgments.** We thank Hans Naus (VU) for useful discussions and for providing  $(\text{O}_2)_2$  absorption cross-sections. We also like to thank P. F. J. van Velthoven (KNMI) for assistance with ECMWF data. ESA is acknowledged for providing GOME data (ESA 1995–1999) processed by DFD/DLR. NSO/Kitt Peak FTS data used here were produced by NSF/NOAO. This work is part of the research program of the “Stichting voor Fundamenteel Onderzoek der Materie (FOM),” which is financially supported by the “Nederlandse organisatie voor Wetenschappelijke Onderzoek (NWO)” and is supported by SRON through project grants EO-023 and EO-046.

### References

- Aben, I., D. M. Stam, and F. Helderma, The Ring effect in skylight polarisation, *Geophys. Res. Lett.*, 28, 519–522, 2001.
- Armstrong, B. H., Spectrum line profiles: The Voigt function, *J. Quant. Spectrosc. Radiat. Transfer*, 8, 61–88, 1967.
- Balzer, W., and D. Loyola, Product specification document of the GOME data processor, Tech. Doc. ER-PS-DLR-60-0016, 21 pp., Dtsch. Forschungsanst. für Luft- und Raumfahrt, Oberpfaffenhofen, Germany, 1996.
- Banks, P. M., and G. Kockarts, *Aeronomy*, Part B, 109 pp., Academic, San Diego, Calif., 1973.
- Bates, D. R., Rayleigh scattering by air, *Planet. Space Sci.*, 32, 785–790, 1984.
- Belmiloud, D., R. Schermaul, K. Smith, N. F. Zobov, F. Nikolai, J. W. Brault, R. C. M. Learner, D. A. Newnham, and J. Tennyson, New studies of the visible and near-infrared absorption by water vapour and some problems with the HITRAN database, *Geophys. Res. Lett.*, 27, 3703–3707, 2000.
- Bovensmann, H., J. P. Burrows, M. Buchwitz, J. Frerick, S. Noël, V. V. Rozanov, K. V. Chance, and A. Goede, SCIAMACHY: Mission objectives and measurement modes, *J. Atmos. Sci.*, 56, 127–150, 1999.
- Buchwitz, M., V. V. Rozanov, and J. P. Burrows, A near-infrared optimized DOAS method for the fast global retrieval of atmospheric  $\text{CH}_4$ ,  $\text{CO}$ ,  $\text{CO}_2$ ,  $\text{H}_2\text{O}$ , and  $\text{N}_2\text{O}$  total column amounts from SCIAMACHY Envisat-1 nadir radiances, *J. Geophys. Res.*, 105, 15,231–15,245, 2000.
- Burrows, J. P., et al., The Global Ozone Monitoring Experiment (GOME): Mission concept and first scientific results, *J. Atmos. Sci.*, 56, 151–175, 1999.
- Byrd, R. H., R. B. Schnabel, and G. A. Shultz, Approximate solution of the trust region problem by minimization over two-dimensional subspaces, *Math. Program.*, 40, 247–263, 1988.
- Carleer, M., A. Jenouvrier, A.-C. Vandaele, P. F. Bernath, M. F. Mérienne, R. Colin, N. F. Zobov, O. L. Polyansky, J. Tennyson, and V. A. Sarin, The near infrared, visible and near ultraviolet overtone spectrum of water, *J. Chem. Phys.*, 111, 2444–2450, 1999.
- Casadio, S., C. Zehner, G. Piscane, and E. Putz, Empirical retrieval of atmospheric air mass factor (ERA) for the measurement of water vapor vertical content using GOME data, *Geophys. Res. Lett.*, 27, 1483–1486, 2000.
- Caspar, C., and K. Chance, GOME wavelength calibration using solar and atmospheric spectra, in *Third ERS Symposium on Space at the Service of our Environment: Florence, Italy, 14–21 March 1997*, Eur. Space Agency Spec. Publ., ESA SP-414, 609–614, 1997.
- Chaboureaud, J.-P., A. Chédin, and N. A. Scott, Remote sensing of the vertical distribution of atmospheric water vapor from the TOVS observations: Method and validation, *J. Geophys. Res.*, 103, 8743–8752, 1998.
- Chance, K., and R. J. D. Spurr, Ring effect studies: Rayleigh scattering, including molecular parameters for rotational Raman scattering, and the Fraunhofer spectrum, *Appl. Opt.*, 36, 5224–5230, 1997.
- de Haan, J., P. Bosma, and J. Hovenier, The adding method for multiple scattering calculations of polarized light, *Astron. Astrophys.*, 181, 371–391, 1987.
- Deutsches Zentrum für Luft- und Raumfahrt (DLR), GOME level 0 to 1 algorithm description, Tech. Note ER-TN-DLR-GO-0025, Dtsch. Fernerkundungszentrum, Oberpfaffenhofen, Germany, 1996.
- Deutsches Zentrum für Luft- und Raumfahrt (DLR), GOME data processor extraction software user's manual, Doc. ER-SUM-DLR-GO-0045, Dtsch. Fernerkundungszentrum, Oberpfaffenhofen, Germany, 1999.
- European Space Agency (ESA), *The Global Ozone Monitoring Experiment User's Manual*, Eur. Space Agency Spec. Publ., ESA SP-1182, edited by F. Bednarz, 1995.
- Filiberti, M.-A., F. Rabier, J. N. Thépaut, L. Eymard, and P. Courtier, Four-dimensional variational assimilation of SSM/I precipitable water content data, *Q.J.R. Meteorol. Soc.*, 124, 1743–1770, 1998.

- Francis, J. A., and A. J. Schweiger, A new window opens on the Arctic, *Eos Trans. AGU*, 81(8), 77, 83, 2000.
- Giver, L. P., J. C. Chackerian, and P. Varanasi, Visible and near-infrared H<sub>2</sub>O line intensity corrections for HITRAN-96, *J. Quant. Spectrosc. Radiat. Transfer*, 66, 101–105, 1999.
- Grainger, J. F., and J. Ring, Anomalous Fraunhofer line profiles, *Nature*, 193, 762, 1962.
- Greenblatt, G. D., J. J. Orlando, J. B. Burkholder, and A. R. Ravishankara, Absorption measurements of oxygen between 330 and 1140 nm, *J. Geophys. Res.*, 95, 18,577–18,582, 1990.
- Hedin, A. E., Extension of the MSIS thermosphere model into the middle and lower atmosphere, *J. Geophys. Res.*, 96, 1159–1172, 1991.
- Koелеmeijer, R. B. A., and P. Stammes, Validation of GOME cloud cover fraction relevant for accurate ozone column retrieval, *J. Geophys. Res.*, 104, 18,801–18,814, 1999.
- Koелеmeijer, R. B. A., P. Stammes, and D. Stam, Spectral surface albedo derived from GOME data, in *Third ERS Symposium on Space at the Service of our Environment: Florence, Italy, 14–21 March 1997, ESA Spec. Publ., SP-414*, 663–667, 1997.
- Learner, R., R. Schermaul, J. Tennyson, N. Zobov, J. Ballard, D. Newnham, and M. Wickett, Measurement of H<sub>2</sub>O absorption cross-sections for the exploitation of GOME data, final presentation, contract 13312/9/NL/SF, Eur. Space Res. and Technol. Cent., Noordwijk, Netherlands, 2000.
- Liou, K.-N., *An Introduction to Atmospheric Radiation*, Academic, San Diego, Calif., 1980.
- Marquard, L. C., T. Wagner, and U. Platt, Improved air mass factor concepts for scattered radiation differential optical absorption spectroscopy of atmospheric species, *J. Geophys. Res.*, 105, 1315–1327, 2000.
- Maurellis, A. N., Non-auroral models of the Jovian ionosphere, Ph.D. thesis, 75 pp., Univ. of Kansas, June 1998.
- Maurellis, A. N., R. Lang, W. J. van der Zande, U. Ubachs, and I. Aben, Precipitable water column retrieval from GOME data, *Geophys. Res. Lett.*, 27, 903–906, 2000a.
- Maurellis, A. N., R. Lang, and W. J. van der Zande, A new DOAS parameterization for retrieval of trace gases with highly-structured absorption spectra, *Geophys. Res. Lett.*, 27, 4069–4072, 2000b.
- Naus, H., and W. Ubachs, Visible absorption bands of the (O<sub>2</sub>)<sub>2</sub>-collision complex at pressures below 760 Torr, *Appl. Opt.*, 38, 3423–3428, 1999.
- Naus, H., W. Ubachs, P. F. Levelt, O. L. Polyansky, N. F. Zobov, and J. Tennyson, Cayity-Ring-Down spectroscopy on water vapor in the range 555–604 nm, *J. Molec. Spectrosc.*, 205, 117–121, 2001.
- Newnham, D. A., and J. Ballard, Visible absorption cross sections and integrated absorption intensities of molecular oxygen (O<sub>2</sub> and O<sub>4</sub>), *J. Geophys. Res.*, 103, 28,801–28,816, 1998.
- Noël, S., M. Buchwitz, H. Bovensmann, R. Hoogen, and J. P. Burrows, Atmospheric water vapor amounts retrieved from GOME satellite data, *Geophys. Res. Lett.*, 26, 1841–1844, 1999.
- Perner, D., and U. Platt, Absorption of light in the atmosphere by collision pairs of oxygen (O<sub>2</sub>)<sub>2</sub>, *Geophys. Res. Lett.*, 7, 1053–1056, 1980.
- Pfeilsticker, K., F. Erle, and U. Platt, Absorption of solar radiation by atmospheric O<sub>4</sub>, *J. Atmos. Sci.*, 54, 933–939, 1997.
- Plane, J. M. C., R. M. Cox, J. Qian, W. M. Pfenninger, G. C. Papen, C. S. Gardner, and P. J. Espy, Mesospheric Na layer at extreme high latitudes in summer, *J. Geophys. Res.*, 103, 6381–6389, 1998.
- Platt, U., Differential optical absorption spectroscopy (DOAS), in *Air Monitoring by Spectroscopic Techniques*, edited by M. W. Sigwist, pp. 27–84, John Wiley, New York, 1994.
- Platt, U., Modern methods of the measurement of atmospheric trace gases, *Phys. Chem. Chem. Phys.*, 1, 5409–5415, 1999.
- Randel, D. L., T. H. Vonder Haar, M. A. Ringerud, G. L. Stephens, T. J. Greenwald, and C. L. Combs, A new global water vapor dataset, *Bull. Am. Meteorol. Soc.*, 77(6), 1233–1246, 1996.
- Richter, A., and J. P. Burrows, A multi wavelength approach for the retrieval of tropospheric NO<sub>2</sub> from GOME measurements, in *ERS-ENVISAT Symposium "Looking Down to Earth in the New Millennium,"* [CD-ROM], Eur. Space Agency Spec. Publ., ESA SP-461, 2000.
- Roscoe, H. K., D. J. Fish, and R. L. Jones, Interpolation errors in UV-visible spectroscopy for stratospheric sensing: Implications for sensitivity, spectral resolution, and spectral range, *Appl. Opt.*, 35, 427–432, 1996.
- Rothman, L. S., et al., The HITRAN Molecular Spectroscopic Database and HAWKS (HITRAN Atmospheric Workstation): 1996 edition, *J. Quant. Spectrosc. Radiat. Transfer*, 60, 665–710, 1998.
- Schrijver, H., Retrieval of carbon monoxide, methane and nitrous oxide from SCIAMACHY measurements, in *ESAMS'99: European Symposium on Atmospheric Measurements From Space, ESA WPP-161*, 285–294, 1999.
- Shettle, E. P., and R. W. Fenn, Models for aerosols of the lower atmosphere and the effects of the humidity variations on their optical properties, Environ. Res. Pap. 676, AFGL-TR-79-0214, Air Force Geophys. Lab. (OP), Hanscom Air Force Base, Mass., 1979.
- Solomon, S., R. W. Portmann, R. W. Sanders, and J. S. Daniel, Absorption of solar radiation by water vapor, oxygen, and related collision pairs in the Earth's atmosphere, *J. Geophys. Res.*, 103, 3847–3858, 1998.
- Thomas, W., E. Hegels, S. Slijkhuys, R. Spurr, and K. Chance, Detection of biomass burning combustion products in Southeast Asia from backscatter data taken by the GOME spectrometer, *Geophys. Res. Lett.*, 25, 1317–1320, 1998.
- Vesperini, M., Humidity in the ECMWF model: Monitoring of operational analyses and forecasts using SSM/I observations, *Q. J. R. Meteorol. Soc.*, 124, 1313–1327, 1998.
- Voigt, S., J. Orphal, K. Bogumil, and J. P. Burrows, The temperature dependence (203–293 K) of the absorption cross sections of O<sub>3</sub> in the 230–850 nm region measured by Fourier-transform spectroscopy, *J. Photochem. Photobiol. A*, 143, 1–9, 2001.
- Vountas, M., V. V. Rozanov, and J. P. Burrows, Ring effect: Impact of rotational Raman scattering on radiative transfer in Earth's atmosphere, *J. Quant. Spectrosc. Radiat. Transfer*, 60, 943–961, 1998.
- Wallace, L., K. Hinkle, and W. Livingston, An atlas of the spectrum of the solar photosphere from 13,500 to 28,000 cm<sup>-1</sup>, N.S.O. Tech. Rep. 98-001, Natl. Opt. Astron. Obs., Tucson, Ariz., June 1998.

I. Aben, J. Landgraf, and A. N. Maurellis, SRON National Institute for Space Research, Sorbonnelaan 2, 3584 CA Utrecht, Netherlands.

R. Lang and W. J. van der Zande, FOM Institute for Atomic and Molecular Physics, Kruislaan 407, 1098 SJ Amsterdam, Netherlands. (r.lang@amolf.nl)

W. Ubachs, Department of Physics and Astronomy, Vrije Universiteit, De Boelelaan 1081, 1081 HV Amsterdam, Netherlands.